

# Multi-Dimensional Optimization of In<sub>0.53</sub>Ga<sub>0.47</sub>As Thermophotovoltaic Cell using Real Coded Genetic Algorithm

**Mansur Gamel**

Universiti Tenaga Nasional

**Pin Jern Ker** (✉ [pinjern@uniten.edu.my](mailto:pinjern@uniten.edu.my))

Universiti Tenaga Nasional

**Hui Jing Lee**

Universiti Tenaga Nasional

**Wan Emilin Suliza Wan Abdul Rashid**

Universiti Tenaga Nasional

**M.A. Hannan**

Universiti Tenaga Nasional

**John David**

University of Sheffield

**Md Zaini Jamaludin**

Universiti Tenaga Nasional

---

## Research Article

**Keywords:** Dimensional Optimization, Genetic Algorithm, Thermophotovoltaic

**Posted Date:** November 25th, 2020

**DOI:** <https://doi.org/10.21203/rs.3.rs-111565/v1>

**License:** © ⓘ This work is licensed under a Creative Commons Attribution 4.0 International License.

[Read Full License](#)

---

**Version of Record:** A version of this preprint was published at Scientific Reports on April 8th, 2021. See the published version at <https://doi.org/10.1038/s41598-021-86175-5>.

## Multi-dimensional Optimization of In<sub>0.53</sub>Ga<sub>0.47</sub>As Thermophotovoltaic cell using Real Coded Genetic Algorithm

Mansur Mohammed Ali Gamel<sup>1</sup> ([mansurgamel@uniten.edu.my](mailto:mansurgamel@uniten.edu.my)),\*Pin Jern Ker<sup>2</sup> ([pinjern@uniten.edu.my](mailto:pinjern@uniten.edu.my)) (+60166395329), Hui Jing Lee<sup>3</sup> ([LHJing@uniten.edu.my](mailto:LHJing@uniten.edu.my)), Wan Emilin Suliza Wan Abdul Rashid<sup>4</sup> ([emilin@uniten.edu.my](mailto:emilin@uniten.edu.my)), M.A. Hannan<sup>5</sup> ([hannan@uniten.edu.my](mailto:hannan@uniten.edu.my)), J. P. R. David<sup>6</sup> ([j.p.david@sheffield.ac.uk](mailto:j.p.david@sheffield.ac.uk)) and M. Z. Jamaludin<sup>7</sup> ([mdzaini@uniten.edu.my](mailto:mdzaini@uniten.edu.my))

\*Correspondence to [pinjern@uniten.edu.my](mailto:pinjern@uniten.edu.my)

<sup>1,2,4,5</sup>Institute of Sustainable Energy, Universiti Tenaga Nasional, 43000 Kajang, Selangor, Malaysia, <sup>3,7</sup>Institute of Power Engineering, Universiti Tenaga Nasional, 43000 Kajang, Selangor, Malaysia, <sup>6</sup>Department of Electronic and Electrical Engineering, The University of Sheffield, Firth Court, Western Bank, Sheffield S10 2TN, United Kingdom

## 1 **Abstract**

2 The optimization of thermophotovoltaic (TPV) cell efficiency is essential since it leads to a  
3 significant increase in the output power. Typically, the optimization of  $\text{In}_{0.53}\text{Ga}_{0.47}\text{As}$  TPV cell has  
4 been limited to single variable such as the emitter thickness, while the effects of the variation in  
5 other design variables are assumed to be negligible. The reported efficiencies of  $\text{In}_{0.53}\text{Ga}_{0.47}\text{As}$   
6 TPV cell mostly remain  $< 15\%$ . Therefore, this work develops a multi-variable or multi-  
7 dimensional optimization of  $\text{In}_{0.53}\text{Ga}_{0.47}\text{As}$  TPV cell using the real coded genetic algorithm  
8 (RCGA) under various radiation temperatures. RCGA was developed using Visual Basic and it  
9 was hybridized with Silvaco TCAD for the electrical characteristics simulation. Under radiation  
10 temperatures from 800 K to 2000 K, the optimized  $\text{In}_{0.53}\text{Ga}_{0.47}\text{As}$  TPV cell efficiency increases by  
11 an average percentage of 11.86% (from 8.5% to 20.35%) as compared to the non-optimized  
12 structure. It was found that the incorporation of a thicker base layer with the back-barrier layers  
13 enhances the separation of charge carriers and increases the collection of photo-generated carriers  
14 near the band-edge, producing an optimum output power of  $0.55 \text{ W/cm}^2$  (cell efficiency of 22.06%,  
15 without antireflection coating) at 1400 K radiation spectrum. The results of this work demonstrate  
16 the great potential to generate electricity sustainably from industrial waste heat and the multi-  
17 dimensional optimization methodology can be adopted to optimize semiconductor devices, such  
18 as solar cell, TPV cell and photodetectors.

## 19 **Introduction**

20 In recent years, thermophotovoltaic (TPV) has been escalating as a promising technology for high  
21 power density generation. A TPV system converts thermal radiations from combustion of fuels,  
22 industrial waste heat, or nuclear energy into electricity. The advantages of noiseless, high  
23 reliability, mechanically stable without moving parts, and large power density, make TPV suitable  
24 for a vast range of real-world applications such as electrical generator<sup>1-3</sup>, aerospace applications<sup>1,4</sup>,  
25 submarine<sup>5</sup>, solar thermophotovoltaic (STPV) cell<sup>6-8</sup>, energy storage<sup>9,10</sup>, waste heat recovery  
26 system in vehicle<sup>11</sup>, metal-alloy industries<sup>2,12,13</sup>, power plant<sup>14,15</sup> and fuel cell<sup>16</sup>. The TPV  
27 converters mainly utilize narrow bandgap (NB) semiconductor materials which allow them to  
28 harvest the maximum amount of infrared radiations (IRs). The advancement of nanotechnology  
29 and material science since 1990s have boosted the development of various NB TPV cells, such as  
30 germanium (Ge)<sup>17</sup>, indium arsenide (InAs)<sup>18</sup>, gallium antimonide (GaSb)<sup>19</sup>, indium gallium

31 arsenide (InGaAs)<sup>20</sup>, indium gallium antimonide (InGaSb)<sup>21</sup>, indium gallium arsenide antimonide  
32 (InGaAsSb)<sup>22</sup> and indium arsenide antimonide phosphate (InAsSbP)<sup>23</sup>. In the last 3 decades of  
33 research in TPV, most researchers focus on the utilization of GaSb cell due to its narrow bandgap  
34 of 0.72 eV. US company JX Crystals Inc has developed a high-performance GaSb TPV cell which  
35 is commercially available and is widely used in various TPV systems<sup>24</sup>. The GaSb TPV cell was  
36 reported to have an efficiency of 29% under radiation temperature of 1548 K<sup>13</sup>. On the other hand,  
37 InGaAs, which has similar bandgap energy and potential in achieving high TPV performance, was  
38 relatively more common for applications in telecommunication and sensing. In<sub>1-x</sub>Ga<sub>x</sub>As is a ternary  
39 semiconductor with bandgap energy ( $E_g$ ) that can be engineered from 1.42 to 0.36 eV by varying  
40 the  $x$  composition of Ga atom, which corresponds to cutoff wavelengths ( $\lambda_c$ ) from 0.87 to 3.34  
41  $\mu\text{m}$ <sup>25</sup>. At  $x = 0.47$ , In<sub>0.53</sub>Ga<sub>0.47</sub>As semiconductor material can be grown lattice-matched on an  
42 indium phosphide (InP) substrate, corresponds to  $E_g$  and  $\lambda_c$  of 0.74 eV and 1.68  $\mu\text{m}$ , respectively.  
43 Moreover, In<sub>0.53</sub>Ga<sub>0.47</sub>As is a promising TPV cell due to its high crystal quality and the cost-  
44 effectiveness of InP substrate, making it suitable for large scale production as compared to other  
45 TPV materials.

46 It is worth mentioning that the existing epitaxy growth technology of metal-organic vapor-phase  
47 epitaxy (MOVPE) has the ability to produce In<sub>0.53</sub>Ga<sub>0.47</sub>As/InP heterojunction with high crystal  
48 quality and low defect density<sup>26,27</sup>. The main structure of In<sub>0.53</sub>Ga<sub>0.47</sub>As configuration includes the  
49 emitter, base, front surface field (FSF), back surface field (BSF), cap and buffer layers. In previous  
50 literature, the base thickness was reported between 1 and 5  $\mu\text{m}$ , and emitter thickness was between  
51 0.05 and 0.44  $\mu\text{m}$ <sup>27-29</sup>. Several structures reported the use of highly doped In<sub>0.53</sub>Ga<sub>0.47</sub>As cap layer  
52  $\sim 1 \times 10^{19} \text{ cm}^{-3}$  and highly doped InP BSF/buffer layer  $\geq 1 \times 10^{18} \text{ cm}^{-3}$ . Table 1 reviews the design  
53 structure and output performances of In<sub>0.53</sub>Ga<sub>0.47</sub>As photovoltaic (PV) cell under different testing  
54 conditions. Typical In<sub>0.53</sub>Ga<sub>0.47</sub>As cells have open-circuit voltage ( $V_{oc}$ ), short circuit current ( $J_{sc}$ ),  
55 fill factor ( $FF$ ) and  $\eta$  ranging between 0.26 to 0.45 V, 18.8 to 64.5  $\text{mA/cm}^2$ , 59 to 74.2%, and 4.2  
56 to 14.37%, respectively under air-mass 0 (AM0) and air-mass 1.5 (AM1.5) illuminations<sup>26,28,30,31</sup>.  
57 In 2019, Omair *et al.*<sup>32</sup> reported a TPV cell efficiency of 29.1% under 1480 K radiation  
58 temperature, by recycling sub bandgap photons to the radiator. It is possible to achieve > 50% cell  
59 efficiency by improving the series resistance, material quality and reflectivity using chamber with  
60 high mirror reflectivity. As summarized in Table 1, the TPV testing conditions resulted in higher  
61 output performance as compared to solar spectrums. Moreover, commercially available TPV cell

62 has the advantage of producing high output power density, ~26 times higher than the output power  
63 of solar PV cell<sup>33,34</sup>. All the reported work in the optimization of In<sub>0.53</sub>Ga<sub>0.47</sub>As cell are based on  
64 the alteration of single design variable<sup>35,36</sup>. Recently, a multi-variable optimization of solar cell  
65 was used to optimize the physical properties of electron transport materials, hole transport  
66 materials, and metal contact and layers thickness. It was accomplished using the MATLAB  
67 optimization toolboxes incorporated with one-dimensional (1D) Solar Cell Capacitance Simulator  
68 (SCAPS) for device simulation<sup>41</sup>. However, the study did not take into account the impact of  
69 doping concentration on the cell performance.

70 **Table 1. Structure design and the performance of reported heterojunction In<sub>0.53</sub>Ga<sub>0.47</sub>As**  
71 **cell.**

Str	Cap thickness (doping)	FSF thickness (doping)	Emitter thickness (doping)	Base thickness (doping)	BSF thickness (doping)	Buffer thickness (doping)	V <sub>oc</sub> (V)	J <sub>sc</sub> (mA/cm <sup>2</sup> )	FF (%)	η (%)	Condition
n-p <sup>26</sup>	0.3 (n/a*)	0.05 (n/a)	0.3 (n/a)	3 (n/a)	0.25 (n/a)	none*	0.35	57.7	71.2	14.3 7	AM1.5
n-p <sup>32</sup>	0.2 (1 × 10 <sup>18</sup> )	0.02 (1 × 10 <sup>18</sup> )	none	2.5 (1 × 10 <sup>17</sup> )	0.1 (1 × 10 <sup>18</sup> )	0.2 (1 × 10 <sup>18</sup> )	0.529	918	73	29.1	1480 K
(n/a) <sub>37</sub>	n/a	n/a	n/a	n/a	n/a	n/a	~0.225	0.5	58	16.4	1323 K
n-p <sup>38</sup>	0.025 (1 × 10 <sup>19</sup> )	0.1 (2 × 10 <sup>18</sup> )	0.1 (5 × 10 <sup>17</sup> )	2.5 (2 × 10 <sup>17</sup> )	0.3 (1 × 10 <sup>18</sup> )	with BSF	0.405	288	65	12.4	0.62 W/cm <sup>2</sup> Tungsten– halogen lamp (3250 K)
p-n <sup>38</sup>	0.025 (1 × 10 <sup>19</sup> )	0.1 (7 × 10 <sup>18</sup> )	2 (1 × 10 <sup>17</sup> )	0.3 (5 × 10 <sup>17</sup> )	0.3 (1.5 × 10 <sup>18</sup> )	with BSF	0.419	284	62	12.1	
n-p <sup>30</sup>	n/a	n/a	0.3 (n/a)	3 (n/a)	n/a	1 (1 × 10 <sup>19</sup> )	0.3 – 0.31	21.5 – 24.9	66 – 70	12.9 – 13.6	AM1.5
n-p <sup>39</sup>	n/a	n/a	0.1 (3 × 10 <sup>17</sup> )	2 (8 × 10 <sup>16</sup> )	n/a	n/a	0.38 & 0.44	5 × 10 <sup>1</sup> & 6 × 10 <sup>2</sup>	n/a	15 & 18	4000 K (0.1 & 1 W/cm <sup>2</sup> )
n-p <sup>40</sup>	none	400 (n/a)	n/a (1 × 10 <sup>19</sup> )	2–4 ((1–5) × 10 <sup>17</sup> )	none	n/a	~0.45– 0.48	~4 × 10 <sup>3</sup>	~69– 72.5	~13. 7–15	1800 K
p-n <sup>41</sup>	0.1 (1 × 10 <sup>19</sup> )	0.07 (1 × 10 <sup>18</sup> )	0.25 (1 × 10 <sup>19</sup> )	1 (undoped)	0.5 (1 × 10 <sup>18</sup> )	n/a	0.341	43.1	68	10.1 1	AM1.5
n-p <sup>28</sup>	n/a	0.05 (1 × 10 <sup>18</sup> )	0.4 (1 × 10 <sup>18</sup> )	3 (4 × 10 <sup>17</sup> )	0.4 (2 × 10 <sup>18</sup> )	none	0.4	45.1	66.9	12.1	AM1.5
n-p <sup>42</sup>	0.3 (1 × 10 <sup>19</sup> )	0.05 (1 × 10 <sup>18</sup> )	0.4 (1 × 10 <sup>18</sup> )	3 ((1–4) × 10 <sup>17</sup> )	0.1 (1 × 10 <sup>18</sup> )	none	0.39	42.8	71	11.8	AM1.5
p-n <sup>43</sup>	0.1 (1 × 10 <sup>19</sup> )	0.1 (2 × 10 <sup>18</sup> )	0.3 (1 × 10 <sup>19</sup> )	2 (5 × 10 <sup>17</sup> )	0.1 (1 × 10 <sup>18</sup> )	1 (2 × 10 <sup>19</sup> )	0.399	56.4	71.5	11.7	AM0
n-p <sup>44</sup>	0.3 (1 × 10 <sup>19</sup> )	0.05 (1 × 10 <sup>19</sup> )	0.1 (1 × 10 <sup>19</sup> )	4 (1 × 10 <sup>17</sup> )	2 (1 × 10 <sup>19</sup> )	none	0.303	9.4	n/a	~1.3 6	1273 K

72 Note: n/a means no data available and none\* represents the unused layer.

73  
74 The optimization of TPV cell structure is critical in getting the highest achievable η. A slight  
75 increment in η will significantly increase the output power and total energy. The simplest method  
76 to optimize a structure is the single-layer/variable optimization, which optimizes only a single

77 parameter at a time while other parameters are kept constant. Several attempts were made to  
78 optimize single variable, especially on the emitter and base layers of  $\text{In}_{0.53}\text{Ga}_{0.47}\text{As}$  cell<sup>35,36</sup>.  
79 However, device performance depends collectively on all the design variables<sup>45,46</sup>, and a more  
80 heuristic optimization that considers the effect of all important variables for the  $\text{In}_{0.53}\text{Ga}_{0.47}\text{As}$  TPV  
81 cell is necessary to achieve the optimum cell efficiency. Therefore, this study investigates the effect  
82 of each variable through single variable optimization and performs multi-dimensional  
83 (simultaneous multi-variables) optimization using real coded genetic algorithm (RCGA) to obtain  
84 the optimum configuration of  $\text{In}_{0.53}\text{Ga}_{0.47}\text{As}$  TPV cell.

### 85 **$\text{In}_{0.53}\text{Ga}_{0.47}\text{As}$ cell Modelling and Validation.**

86 The  $\text{In}_{0.53}\text{Ga}_{0.47}\text{As}$  cell was modeled using the computational numerical modeling TCAD Silvaco  
87 ATLAS software package. A 2-dimensional (2D)  $\text{In}_{0.53}\text{Ga}_{0.47}\text{As}$  model was constructed using  
88 DevEdit tool, while the computations on the electrical characteristics were mainly performed with  
89 ATLAS. The input-output transformation method is used to validate the  $\text{In}_{0.53}\text{Ga}_{0.47}\text{As}$  simulation  
90 model with similar experimental work reported by Sodabanlu *et al.*<sup>27</sup>. The input parameters are  
91 structure design and testing conditions. The structure design includes front and back gold contacts,  
92 thickness and doping concentration of the emitter, base, BSF, FSF, buffer and cap layers, as shown  
93 in Fig. 1a. No anti-reflective coating (ARC) was considered in the structure. The validation testing  
94 is performed under a standardized solar spectrum AM1.5 at room temperature (300 K). The output  
95 performance parameters that are of primary interest include IV-curve,  $J_{sc}$ ,  $V_{oc}$ ,  $FF$  and  $\eta$ . The  
96 simulation took into consideration the Auger, radiative and Shockley–Read–Hall (SRH)  
97 recombination as well as the carrier’s lifetime and mobility concentration-dependent models. At a  
98 doping concentration of  $1 \times 10^{17} \text{ cm}^{-3}$ , lifetime of 16 ns for electrons and 40 ns for holes were used  
99 based on the model. While the  $\text{In}_{0.53}\text{Ga}_{0.47}\text{As}$  model and testing conditions remain constant over  
100 the validation process, the materials parameters of the  $\text{In}_{0.53}\text{Ga}_{0.47}\text{As}$  and InP were varied within  
101 the reported range in previous literature. Table 2 summarizes the electrical properties of  $\text{In}_{1-x}\text{Ga}_x\text{As}$   
102 as a function of  $x$  composition and concentration-dependent models.

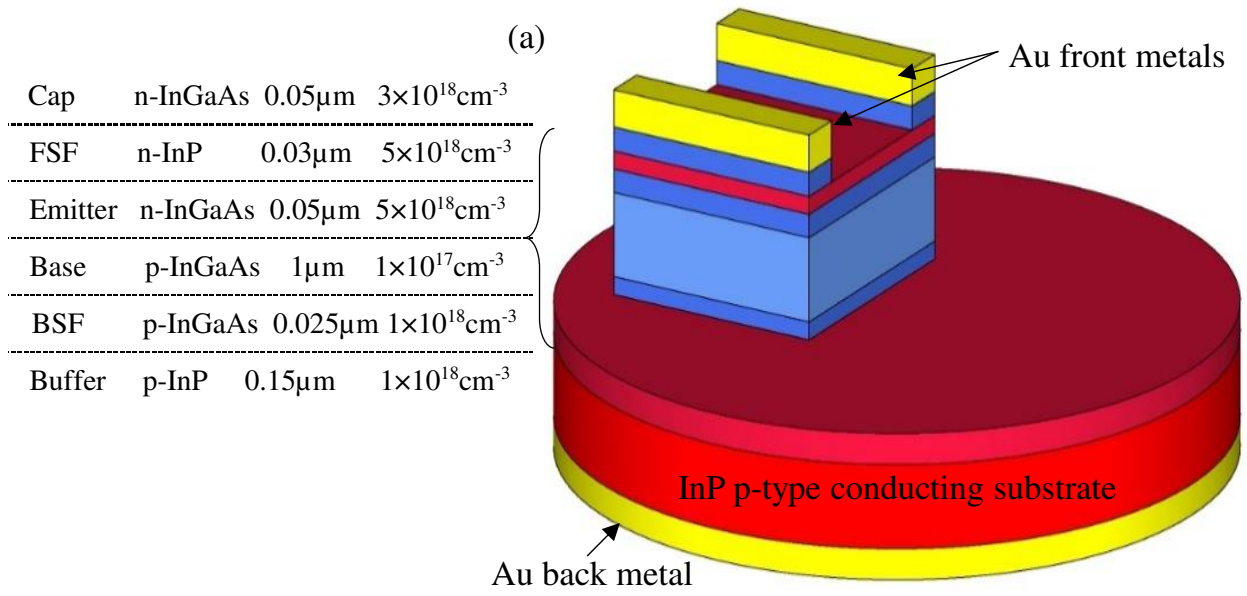
**Table 2. Material parameters of In<sub>1-x</sub>Ga<sub>x</sub>As and In<sub>0.53</sub>Ga<sub>0.47</sub>As at 300 K.**

Material properties at 300 K	(x) is the composition & (N) is the doping level	Range	Numerical values determined in this work
Bandgap <sup>26,48,49</sup> $E_g$ (eV)	$E_g(x) = 0.436x^2 + 0.629x + 0.39$	0.734 – 0.77	0.75
Affinity <sup>26,48,49</sup> $E_{ea}$ (eV)	$E_{ea}(x) = 4.9 - 0.83x$	4.47 – 4.5	4.47
Permittivity <sup>26,48</sup> $\epsilon$	$\epsilon(x) = 0.67x^2 - 2.87x + 15.1$ (static) $\epsilon(x) = 12.3 - 1.4x$ (high frequency)	11.6 – 13.899	13.8
Electron density of states <sup>26,48</sup> $N_c$ (cm <sup>-3</sup> )	$N_c(x) = 2.289 \times 10^{17} x^2 + 1.541 \times 10^{17} x + 8.7 \times 10^{16}$ $N_c(x) = 2 \left( \frac{2\pi m_e \times kT}{h^2} \right)^{3/2}$	$2.1 \times 10^{17}$	$2.1 \times 10^{17}$
Hole density of states <sup>26,48</sup> $N_v$ (cm <sup>-3</sup> )	$N_v(x) = 1.124 \times 10^{17} x^2 + 2.288 \times 10^{18} x + 6.6 \times 10^{18}$ $N_v(x) = 2 \left( \frac{2\pi m_h \times kT}{h^2} \right)^{3/2}$	$7.7 \times 10^{18}$	$7.7 \times 10^{18}$
Electron Mobility <sup>26,47,50-52</sup> $\mu_e$ (cm <sup>2</sup> V <sup>-1</sup> s <sup>-1</sup> )	$\mu_e(x) = (40 - 80.7x + 49.2x^2) \times 1000$ $\mu_h \cong 300 / 400$	3372 – 14000	$\mu_{max} = 11599$ $\mu_{min} = 3372$ $N_{ref} = 2.1 \times 10^{17} \text{ cm}^{-3}$ $z = 0.76$
Hole Mobility <sup>26,47,50-52</sup> $\mu_h$ (cm <sup>2</sup> V <sup>-1</sup> s <sup>-1</sup> )	$\mu_{e,h}(N) = \mu_{e,h(min)} + \frac{\mu_{e,h(max)} - \mu_{e,h(min)}}{1 + (N_{D,A} / N_{ref(e,h)})^z}$	10 – 331	$\mu_{max} = 331$ $\mu_{min} = 75$ $N_{ref} = 7.7 \times 10^{18} \text{ cm}^{-3}$ $z = 1.37$
Electron Lifetime <sup>26,47,50,53-57</sup> $\tau_e$ (sec)	$\tau_{e,h}(N) = (2.11 \times 10^4 + 1.443 \times 10^{-10} N + 8.1 \times 10^{-29} N^2)^{-1}$ $\tau_{e,h}(N) = \frac{\tau_{0(e,h)}}{1 + (N_{D,A} / N_{ref(e,h)})^\gamma}$	$0.05 \times 10^{-9} - 55 \times 10^{-6}$	$\tau_0 = 16 \times 10^{-9}$ $\gamma = 0.73$ $N_D = 1 \times 10^{17} \text{ cm}^{-3}$
Hole Lifetime <sup>26,47,50,53-57</sup> $\tau_h$ (sec)		$0.1 \times 10^{-9} - 90 \times 10^{-6}$	$\tau_0 = 40 \times 10^{-9}$ $\gamma = 1.2$ $N_A = 1 \times 10^{17} \text{ cm}^{-3}$
Auger recombination <sup>26,47,49,53,55</sup> $R_{Aug}$	$R_{Aug} = (C_n + C_p p)(np - n_i^2)$	$3.2 \times 10^{-28} - 8 \times 10^{-29}$ $3.2 \times 10^{-28} - 7 \times 10^{-29}$	$C_n = C_p = 8.1 \times 10^{-29} \text{ cm}^{-6} \text{ s}^{-1}$
Radiative recombination <sup>26,47,49,55</sup> $R_{Rad}$	$R_{Rad} = \frac{C}{4} (np - n_i^2)$	$0.96 \times 10^{-10} - 9.6 \times 10^{-11}$	$C = 0.96 \times 10^{-10} \text{ cm}^3/\text{s}$

104 Note: \*z represents mobility fitting parameter, \* $\gamma$  represents lifetime fitting parameter, \* $C_{n,p}$  are electron and hole radiative coefficient, \*C is auger  
105 coefficient, \*n is hole densities, \*p represents hole densities,  $N_{D,A}$  doner and acceptor doping concentration and \* $n_i$  represents intrinsic region.

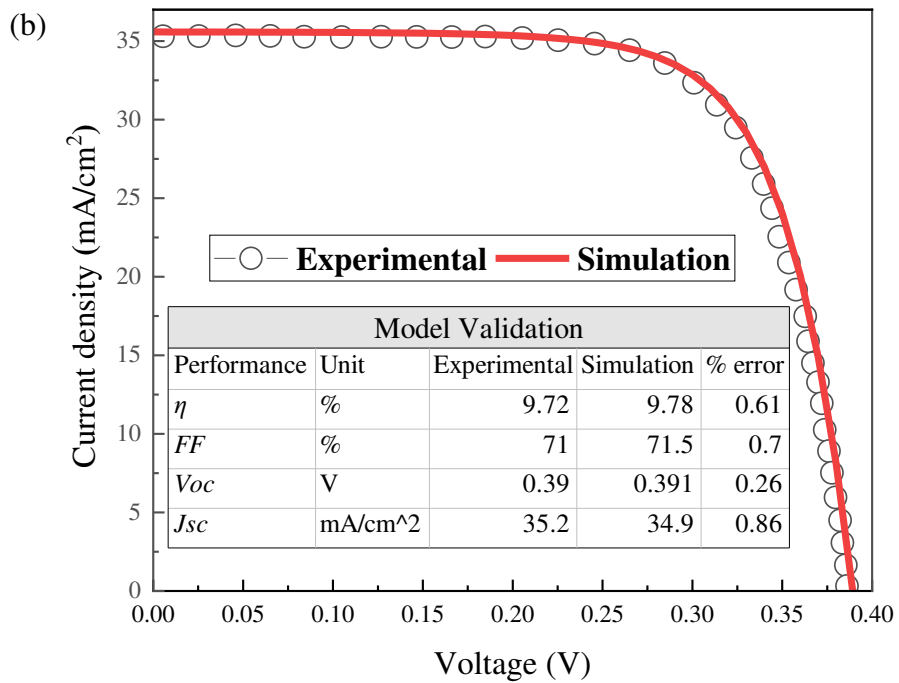
106

107 Using the identified material parameters in Table 2, the current density-voltage (JV) characteristics  
108 of the In<sub>0.53</sub>Ga<sub>0.47</sub>As cell are obtained. The generated JV characteristics of the simulation model  
109 can be seen in Fig. 1b. It can be observed that a close agreement was obtained between the  
110 performance parameters of the simulation model and the reported experimental data. A percentage  
111 error of less than 1% was achieved for each parameter. For example, a percentage error of 0.61%  
112 between the experimental and simulation results was calculated for  $\eta$ . In addition, it was reported  
113 by other literature that the performance parameters of  $\eta$ ,  $FF$ ,  $V_{oc}$  and  $J_{sc}$ , under similar testing  
114 condition (AM1.5), were in the range of 9.3 to 12.9%, 68 to 71%, 0.31 to 0.39 V and 21.5 to 42.8  
115 mA/cm<sup>2</sup>, respectively<sup>30,41,42</sup>. The simulation results for the validation work achieved in this study  
116 are within the reported range; hence, validate the In<sub>0.53</sub>Ga<sub>0.47</sub>As cell model in this work.



117

118



119

120 Figure 1. Simulation to reported experimental of  $\text{In}_{0.53}\text{Ga}_{0.47}\text{As}$  (a) Baseline n-p structure<sup>27</sup> (b) JV

121

curve and performance parameters.

122

123 **Single Layer/Variable Optimization.**

124 A single variable optimization gives an indication of the significance of a variable to the TPV cell  
 125 performance, reveals the trend of performance variation for each variable and more importantly it  
 126 identifies the range of the design parameters accurately, and that provides the RCGA with a much  
 127 faster convergence speed as well as a higher solution accuracy. Based on the reported values for  
 128 the thickness and doping concentration of each layer in Table 1, their maximum and minimum  
 129 values were first estimated. However, since the majority of the  $\text{In}_{0.53}\text{Ga}_{0.47}\text{As}$  structures are used  
 130 for PV application, several simulations were conducted to modify the upper and lower boundary  
 131 conditions to suit TPV testing conditions. Table 3 shows the range of the design parameters for  
 132 the  $\text{In}_{0.53}\text{Ga}_{0.47}\text{As}$  TPV cell. Individually, each variable was manipulated while the rest of the  
 133 design parameters in Fig. 1a remained constant. In the BSF analysis, base thickness was fixed at  
 134  $10\ \mu\text{m}$  to reduce the absorption in BSF, thereby allowing the investigation of the layer functionality  
 135 as field generator. The optimization process was conducted under radiation temperatures from 800  
 136 to 2000 K at 50% beam illumination intensity. The 50% beam intensity was preferred as selective  
 137 radiator usually emitted  $\sim 50\%$  less power than an ideal blackbody<sup>58</sup>. In addition, a low pass optical  
 138 filter at  $2\ \mu\text{m}$  was employed in the simulation following the reported TPV system<sup>59-61</sup>. Fourspring  
 139 *et al.*<sup>62</sup> illustrated the use of the edge short-pass filter and emphasized that the optical interference  
 140 material has high spectral efficiency which reduces the amount of energy that reaches the TPV cell  
 141 for wavelengths higher than  $2\ \mu\text{m}$ .

142 **Table 3. The range of thicknesses and doping concentrations for the single variable**  
 143 **optimization  $\text{In}_{0.53}\text{Ga}_{0.47}\text{As}$  structure.**

$\text{In}_{0.53}\text{Ga}_{0.47}\text{As}$ cell	Thickness Range ( $\mu\text{m}$ )	Doping Concentration Range ( $\text{cm}^{-3}$ )
Cap Layer	0.01 – 0.3	$1 \times 10^{16} - 5 \times 10^{20}$
FSF Layer	0.01 – 0.3	$1 \times 10^{16} - 5 \times 10^{20}$
Emitter layer	0.02 – 0.3	$1 \times 10^{16} - 1 \times 10^{19}$
Base Layer	1 – 30	$5 \times 10^{16} - 1 \times 10^{19}$
BSF Layer	0.02 – 1	$1 \times 10^{16} - 5 \times 10^{19}$
Buffer Layer	0.02 – 3	$1 \times 10^{19} - 1 \times 10^{20}$

144

145 **Multi-dimensional Optimization using Real Coded Genetic Algorithm Method.**

146 The multi-dimensional optimization performs complete iterations for all possible combination of  
 147 different variables to obtain the optimum values for all variables that achieve the highest  
 148 efficiency. A flow chart of the multi-variable optimization of  $\text{In}_{0.53}\text{Ga}_{0.47}\text{As}$  structure under  
 149 different radiation temperatures is presented in Fig. 2. The optimization process consists of both  
 150 the device simulation module and the numerical optimization. Firstly, the device simulation  
 151 module, where ATLAS was used to simulate the 2D  $\text{In}_{0.53}\text{Ga}_{0.47}\text{As}$  model. An initial population  
 152 size of 50 input vector  $X$  was implemented in the final optimization version. It was demonstrated  
 153 that a higher population size improves the accuracy and reduces the number of generation (Gen)  
 154 required to allow the iterations to converge to the optimum  $\text{In}_{0.53}\text{Ga}_{0.47}\text{As}$  configuration.  $X$  is given  
 155 in Equation (1) as the six-layer/twelve design variables to be optimized.

$$156 \quad X = X_i = [x_{i1}, x_{i2}, \dots, x_{in}] = [x_{i1}, x_{i2}, \dots, x_{i12}] \quad (1)$$

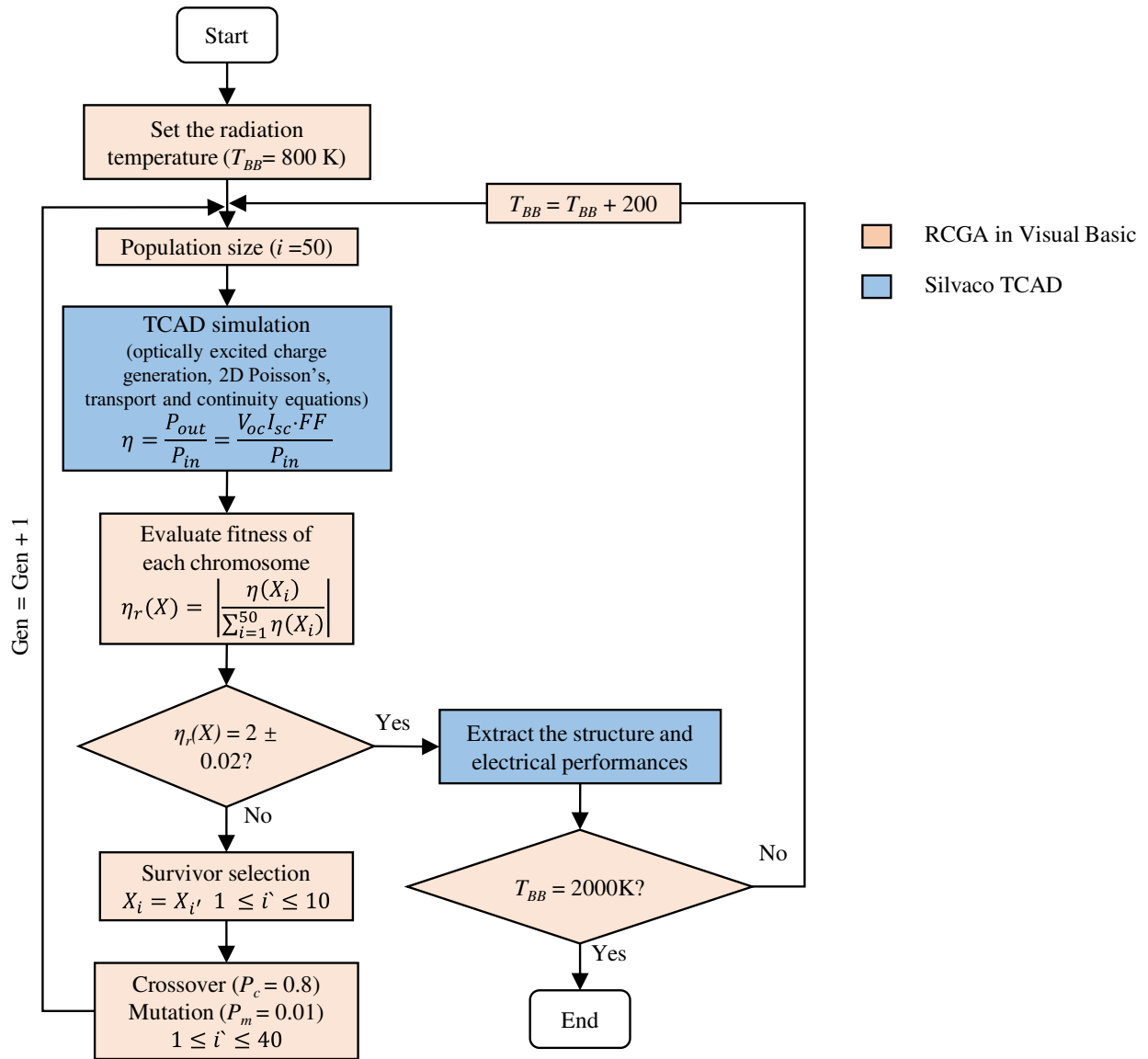
157 where  $i = 1$  to 50 is the initial population size,  $n = 1$  to 12 is the design variables based on some  
 158 lower and upper physical constraints  $x_L \leq x_{in} \leq x_U$  in Table 4. DBinternal tool is used to  
 159 interfaced 50 sets of  $X$  to Deckbuild ATLAS, then solves the optically excited charge generation,  
 160 2D Poisson's Equation, transport Equation, and continuity Equations and calculates the efficiency  
 161 ( $\eta(X)$ ) of the cell based on the inputs. Moreover, the numerical optimization of RCGA method was  
 162 performed. Real coded is a direct representation of the variables, where no coding and encoding is  
 163 required<sup>63</sup>. The objective function is to maximize the  $\eta$  of the  $\text{In}_{0.53}\text{Ga}_{0.47}\text{As}$  TPV cell, as presented  
 164 in Equation (2).

$$165 \quad \eta_{\max} = \max_{x_L \leq x_{in} \leq x_U} \eta(X) \quad (2)$$

166 where  $\eta$  is

$$167 \quad \eta = \frac{P_{out}}{P_{in}} = \frac{V_{oc} J_{sc} FF}{P_{in}} \quad (3)$$

168 where  $P_{in}$  is the TPV illumination intensity under radiation temperatures ranging from 800 to 2000  
 169 K, and  $P_{out}$  is the output electrical power.



170

171

172

173

Figure 2. The flowchart that illustrates the hybridization of Silvaco TCAD with Real coded genetic algorithm.

174 **Table 4. The variables upper and lower boundary conditions for the multi-dimensional**  
 175 **optimization In<sub>0.53</sub>Ga<sub>0.47</sub>As structure.**

In <sub>0.53</sub> Ga <sub>0.47</sub> As cell	Thickness (μm)		Doping concentration (cm <sup>-3</sup> )	
	Lower limit ( $x_L$ )	Upper limit ( $x_U$ )	Lower limit ( $x_L$ )	Upper limit ( $x_U$ )
Cap Layer	0.02	0.14	$8 \times 10^{17}$	$6 \times 10^{19}$
FSF Layer	0.02	0.14	$8 \times 10^{17}$	$6 \times 10^{19}$
Emitter layer	0.05	0.32	$5 \times 10^{16}$	$7 \times 10^{18}$
Base Layer	2.00	20.0	$8 \times 10^{17}$	$6 \times 10^{19}$
BSF Layer	0.02	0.14	$8 \times 10^{17}$	$6 \times 10^{19}$
Buffer Layer	0.02	0.14	$8 \times 10^{17}$	$6 \times 10^{19}$

176

177 The fitness ratio is defined as the efficiency ratio ( $\eta_r(X)$ ), and it is shown in Equation (4). The  
 178 chromosomes are arranged based on their fitness from higher to lower ( $i' = 1$  to 50), and then some  
 179 evolution mechanisms like survivor selection, crossover and mutation were used to build the next  
 180 generation (Gen) using Excel and Visual basic. A 20% (10-best fitted chromosomes:  $X_i = X_I$  to  
 181  $X_{I0}$ ) of the best chromosomes survived and directly passed to the next Gen as  $X_{i'}$  while 80% (40-  
 182 best fitted chromosomes) of the best-selected chromosomes go to the next step of crossover and  
 183 mutation producing a new set of population<sup>64</sup>. This process is presented in Equation (5).

$$184 \quad \eta_r(X) = \left| \frac{\eta_r(X_i)}{\sum_{i=1}^{50} \eta_r(X_i)} \right| \quad (4)$$

$$185 \quad \left\{ \begin{array}{ll} X_i = X_{i'} & 1 \leq i' \leq 10 \\ p_c = 0.8, p_m = 0.01 & 1 \leq i' \leq 40 \\ X_i = 0 & i' > 40 \end{array} \right. \quad (5)$$

186 After some Gen's simulations, child chromosomes were created from the best performing parent  
 187 chromosomes producing the optimum In<sub>0.53</sub>Ga<sub>0.47</sub>As configuration. A stopping criterion was  
 188 decided after observing no significant change in the efficiency and efficiency ratio within the Gen  
 189 ( $\eta_r(X) = 2 \pm 0.3$ ). In this way, the optimization process was repeated for illumination source  
 190 temperatures from 800 K to 2000 K, with an interval of 200 K.

191 **Results and Discussion.**

192 **Single Layer/Variable Optimization.**

193 The effect of varying the thickness and doping concentration of cap, FSF, emitter, base, BSF and  
 194 buffer layers on the performance parameters ( $J_{sc}$ ,  $V_{oc}$ ,  $FF$ ,  $\eta$ ) are tabulated in Table 5. The variables  
 195 are classified into three categories: Insignificant where the variation in  $\eta$  is  $\leq 0.4\%$ , significant  
 196 where the change in  $\eta$  is between  $0.4\%$  and  $3\%$  and highly significant where the change in  $\eta$  is  $\geq$   
 197  $3\%$ .

198 **Table 5. The summary of the result for single variable optimization for blackbody**  
 199 **temperature from 800 K to 2000 K.**

Designing variables	Optimum range	Output parameters				Designing variables
		$\eta$	$FF$	$V_{oc}$	$J_{sc}$	
Cap thickness	$\sim 0.02$	√	√	√	×	Significant for all $T_{BB}$
Cap doping	$> 1 \times 10^{19}$	√	√	×	×	Significant for $T_{BB} > 1000$ K
FSF thickness	$< 0.09$	√	√	√	×	Significant for $T_{BB} < 1400$ K
FSF doping	$> 5 \times 10^{18}$	×	×	×	×	Insignificant for all $T_{BB}$
Emitter thickness	$0.1 - 0.16$	√	√	√	√	Significant for all $T_{BB}$
Emitter doping	$2 - 3 \times 10^{17}$	√	√	√	×	Significant for $T_{BB} < 1400$ K
Base thickness	$5 - 16$	√	√	√	√	Highly significant for all $T_{BB}$
Base doping	$3 - 6 \times 10^{17}$	√	√	√	√	Significant for all $T_{BB}$
BSF thickness	$\sim 0.025$	√	√	×	√	Highly significant at 2000 K and significant for $1600 \text{ K} \leq T_{BB} < 1800$ K
BSF doping	$\sim 1 \times 10^{18}$	×	×	×	×	Insignificant for all $T_{BB}$
Buffer thickness	$< 0.4$	√	√	√	×	Significant for all $T_{BB}$
Buffer doping	$> 1 \times 10^{19}$	√	√	×	×	Significant and more significant for $T_{BB} > 800$ K

200 Note: √ Changing the variable affects the output parameter (percentage improvement by  $\pm \geq 1\%$ )  
 201 and × Changing the variable does not affect the output parameter (percentage improvement by  $\pm$   
 202  $< 1\%$ ).

203

204 As can be seen from Table 5, the  $V_{oc}$  is not significantly affected by the doping concentration of  
 205 the cap, FSF, BSF and buffer layers. Theoretically,  $V_{oc}$  is influenced by dark current densities ( $J_{01}$   
 206 and  $J_{02}$ ), where  $J_{01}$  is contributed to the dark current due to surface and bulk recombination losses,  
 207 and  $J_{02}$  is related to recombination due to traps in the space charge region (SCR)<sup>65</sup>. However, the  
 208 implementation of InP in the front and rear side of the junction reduces the front surface  
 209 recombination and back surface recombination, eliminating the dark current across the surface.

210 The variation of cap, FSF, BSF and buffer doping concentration produces no effect on the  $V_{oc}$  of  
211 the cell since no absorption and recombination have occurred. This is because the Type-II band  
212 alignment (staggered band) between InP/In<sub>0.53</sub>Ga<sub>0.47</sub>As and In<sub>0.53</sub>Ga<sub>0.47</sub>As /InP led to spatial  
213 separation of electrons and holes and passivated the surfaces<sup>66</sup>. However, the thickness increment  
214 of those layers will affect the  $V_{oc}$  because of the losses due to the light absorption<sup>67</sup>.

215 The  $J_{sc}$  is mainly related to the absorption and diffusion length of the photo-generated carriers, as  
216 shown in Equation (6)<sup>68</sup>.

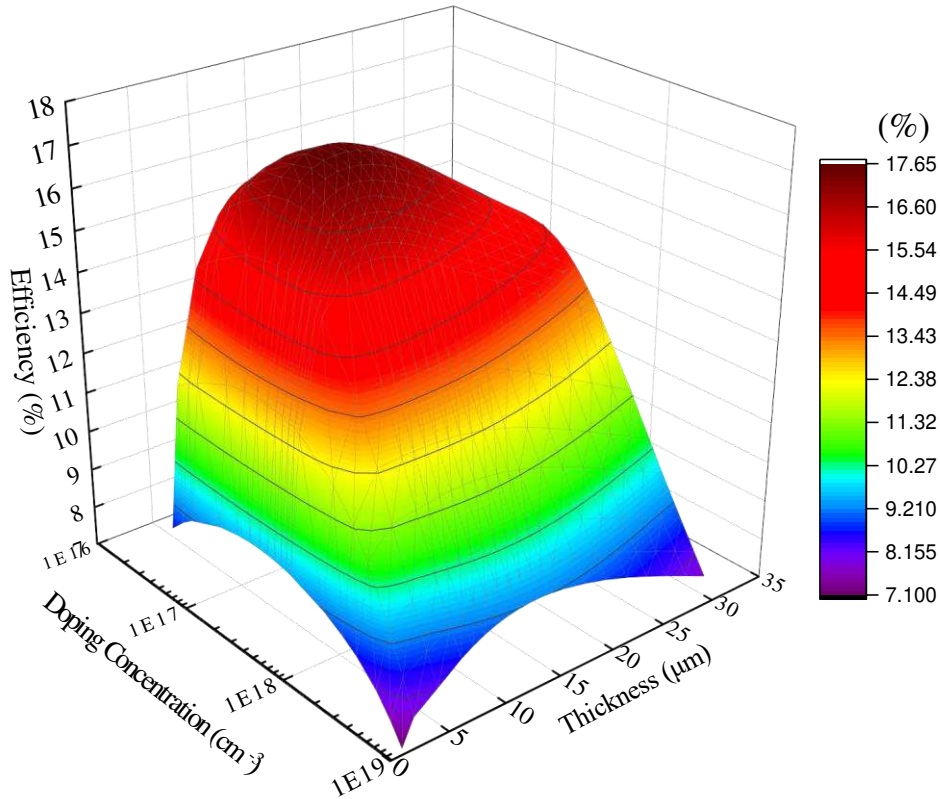
$$217 \quad I_{sc} = qG(L_n + L_p) \quad (6)$$

218 where  $G$  is the generation rate,  $q$  is the charge, and  $L_n$  and  $L_p$  are the electron and hole diffusion  
219 length, respectively.

220 Since In<sub>0.53</sub>Ga<sub>0.47</sub>As material has a long electron and hole diffusion lengths, the increment of  
221 emitter, base and BSF thicknesses will significantly improve the absorption, carrier's generation  
222 and  $J_{sc}$ . For instance, the generated electrons (holes) at absorber layers has a diffusion length of  
223 18.89 (5.88)  $\mu\text{m}$  at  $1 \times 10^{17} \text{ cm}^{-3}$  doping concentration. The increment of base layer thickness from  
224 1 to 18.89  $\mu\text{m}$  will increase the  $J_{sc}$  since majority of the generated minority carriers (electrons) are  
225 able to reach the SCR before they are recombined. The doping concentrations of the absorber  
226 (emitter, base and BSF layers) affect the probability of carrier recombination as the mobility,  
227 lifetime and diffusion length of carriers decrease with higher doping concentration. However, since  
228 the emitter layer and BSF layer were remained constant at 0.05  $\mu\text{m}$  and 0.025  $\mu\text{m}$ , the variation of  
229 doping concentration gives a minor effect on the cell  $J_{sc}$ .

230 The  $FF$  is defined as the ratio between the  $V_{oc}I_{sc}$  to the actual operating condition of the cell  $P_{mp} =$   
231  $I_{mp}V_{mp}$  after considering the series resistance and shunt resistance in the structure<sup>69</sup>. The  $P_{mp}$ ,  $I_{mp}$   
232 and  $V_{mp}$  are denoted as the cell maximum power, maximum current and maximum voltage,  
233 respectively. It can be seen that the  $FF$  and  $\eta$  performance parameters were affected by almost all  
234 of the design variables. This is due to the domination of resistance losses when manipulating the  
235 variable individually. Nevertheless, the manipulation of FSF and BSF doping concentration had  
236 no significant impact on cell performance since the thickness of those layers are kept at very thin  
237 ( $\sim 0.02 \mu\text{m}$ ), resulting in lower resistance losses and minor absorption.

238 Based on the single variable optimization, it was found that the manipulation of the thickness and  
239 doping concentration variables for the base layer significantly affects all performance parameters.  
240 In particular, the highest simulated  $\eta$  is achieved at an optimum base layer thicknesses of 5 and 16  
241  $\mu\text{m}$  with a blackbody temperature of 2000 K and 800 K, respectively. The variation of the optimal  
242 base thicknesses is related to the radiation spectrum and its peak wavelength ( $\lambda_p$ ). Based on Wien's  
243 displacement law,  $\lambda_p$  of the spectrum shifts toward shorter IRs for higher blackbody temperature  
244 hence thinner base layer is required. Low doping in the base layer led to a high minority carrier  
245 lifetime and long diffusion length, which could increase the probability of carriers reaching the  
246 contact before recombining. However, it could also reduce the conductivity of the layer, electric  
247 field, and the built-in potential at the junction that decreases the  $V_{oc}$  performance, offsetting the  
248 improvement in  $J_{sc}$ . On the other hand, a thicker base layer will increase the absorption of IRs,  
249 which results in higher  $J_{sc}$ . However, it could also increase the recombination and shunt  
250 resistance<sup>70,71</sup>. Increasing the thickness is detrimental to cell performance since it causes higher  
251 recombination, especially if the structure has high SRH rate<sup>72</sup>. Moreover, the minority carriers  
252 generated in the lower region of the cell with diffusion length shorter than the thickness has a  
253 higher probability of recombining before reaching the SCR<sup>70</sup>. Therefore, it is worth exploring the  
254 tradeoff relationship of the base layer thicknesses and doping concentrations to acquire the  
255 optimum configuration of the base layer that produces the highest cell efficiency. The correlation  
256 of cell efficiency with the base layer thickness and base doping concentration is depicted in Fig.  
257 3. The base thickness (doping concentration) was varied between 1 ( $6 \times 10^{16}$ ) and 28  $\mu\text{m}$  ( $1 \times 10^{19}$   
258  $\text{cm}^{-3}$ ), while the rest of structure design variables were kept at their baseline values.



259  
 260 Figure 3. The efficiency of  $\text{In}_{0.53}\text{Ga}_{0.47}\text{As}$  TPV cell vs thickness and doping concentration of the  
 261 base layer under 1400 K blackbody temperature.

262  
 263 Based on Fig. 3, it was found that an optimum  $\eta$  of 17.61% is obtained at an optimum base  
 264 thickness (doping concentration) of 11  $\mu\text{m}$  ( $1 \times 10^{17} \text{ cm}^{-3}$ ). The increment in base thickness  
 265 improves the absorption of IR, especially the band-edge photons<sup>72</sup>. Based on the Einstein  
 266 relationship, Caughey-Thomas model and SRH model, the diffusion length of electron and hole  
 267 are calculated as a function of doping concentration. At base doping of  $1 \times 10^{17} \text{ cm}^{-3}$ , the diffusion  
 268 length of electron (hole) is equal to 18.89 (5.88)  $\mu\text{m}$ . The electron diffusion length of 18.89  $\mu\text{m}$  is  
 269 longer than the 11  $\mu\text{m}$  base thickness. Since the diffusion length is longer than the base thickness,  
 270 the probability that photo-generated carriers can reach the SCR is quite high<sup>70</sup>. Furthermore, the  
 271 high diffusion coefficient of  $\text{In}_{0.53}\text{Ga}_{0.47}\text{As}$  carriers permits the formation of the active junction at  
 272 low doping concentration.  $\text{In}_{0.53}\text{Ga}_{0.47}\text{As}$  cell ability to produce active junction at low doping  
 273 concentration allows it to obtained high cell efficiency with minimum recombination rate.

274 **Multi-dimensional Optimization using Real Coded Genetic Algorithm Method.**

275 The results of RCGA optimization on  $\text{In}_{0.53}\text{Ga}_{0.47}\text{As}$  TPV cell model under 800 K to 2000 K  
276 blackbody temperatures are summarized in Table 6. It was found that the optimized cell presented  
277 in this work has thicker base layer as compared to those TPV cells reported in Table 1. At 1800 K  
278 blackbody temperature, the optimized cell has an efficiency of 20.48%, compared to 15% reported  
279 for TPV cell tested under similar testing conditions<sup>40</sup>. A thicker base layer between 16 to 18  $\mu\text{m}$  is  
280 preferred to enhance the current density as it increases the absorption of near band-edge photons  
281 and free-carrier absorption (FCA), which highly impact TPV cell efficiency<sup>73,74</sup>. At base layer  
282 thickness of 16 to 18  $\mu\text{m}$ , the maximum cell efficiency of 23.18% was reported at 1400 K radiation  
283 temperature, while the minimum efficiency of 18.41% was achieved at 800 K. However,  
284 considering the technical difficulties and cost in growing high-quality  $\text{In}_{0.53}\text{Ga}_{0.47}\text{As}$  layer at  $> 10$   
285  $\mu\text{m}$ , the base layer thickness was reduced to 8  $\mu\text{m}$ . With this reduction in base layer thickness, the  
286 efficiency of the TPV cell is reduced only by an average of 1% (Maximum reduction of 1.9% at  
287 1000 K and minimum reduction of 0.1% at 2000 K). A thinner cap and buffer layers are designed  
288 with a higher doping concentration to form a better front and rear ohmic contacts, resulting in  
289 higher  $FF$  and lower series resistance. Besides, a thin FSF and BSF layers are designed with a  
290 higher doping concentration, resulting in a better front and rear junction passivation with minimum  
291 optical absorption.

292 A proper cell design has to consider both optical and electronic losses. The  $\text{In}_{0.53}\text{Ga}_{0.47}\text{As}$  TPV cell  
293 has to be optically thick (i.e. to absorb all or most of the incident illumination) and electronically  
294 thin (i.e. to collect the photoexcited electron-hole pairs with little or no losses). These two  
295 requirements lead to an optimal configuration that maximizes efficiency. At 1400 K blackbody  
296 temperature,  $J_{sc}$  and  $FF$  are increased respectively from 755.01 to 1719.35  $\text{mA}/\text{cm}^2$  and 62.65 to  
297 68.63% after optimizing the entire cell configuration. Most of the optimization works focused on  
298 optimizing the electrical losses of cell to improve the  $V_{oc}$  performance by reducing the thickness  
299 of the absorber layer<sup>27,76</sup>. However, the absorption of near band-edge photons is neglected. Alharbi  
300 *et al.*<sup>77</sup> highlighted that the leading cause of the reduced efficiency of a solar cell below the  
301 theoretical limit is the drop in the estimated  $V_{oc}$  while usually, the obtained  $J_{sc}$  is around the  
302 theoretically maximum values. It is important to mention that the solar spectrum is mainly  
303 concentrated around the visible region, and these photons do not require thicker base absorber. On  
304 the other hand, TPV illumination flux is usually concentrated at infrared wavelengths, and thicker

305 absorber is needed to improve the absorption of IRs and significantly increase  $J_{sc}$ . This statement  
 306 was supported by the optimization study reported by Baudrit and Algora<sup>46</sup>, where increasing the  
 307 absorber thickness of the bottom cell in GaInP/GaAs dual-junction increases the value of  
 308 photocurrent density. Furthermore, the  $J_{sc}$  and  $\eta$  were increased respectively from 13.85 to 15.62  
 309 A/cm<sup>2</sup> and 32.6 to 36.4% under 1000 suns concentration.

310 **Table 6. The optimum In<sub>0.53</sub>Ga<sub>0.47</sub>As TPV configuration from real coded genetic algorithm**  
 311 **method.**

$T_{BB}$ (K)	In <sub>0.53</sub> Ga <sub>0.47</sub> As cell												Performance			
	Cap Layer		FSF Layer		Emitter layer		Base Layer		BSF Layer		Buffer Layer		$V_{oc}$ (V)	$J_{sc}$ (mA/cm <sup>2</sup> )	$FF$ (%)	$\eta$ (%)
	Thickness ( $\mu\text{m}$ )	Doping (cm <sup>-3</sup> )	Thickness ( $\mu\text{m}$ )	Doping (cm <sup>-3</sup> )	Thickness ( $\mu\text{m}$ )	Doping (cm <sup>-3</sup> )	Thickness ( $\mu\text{m}$ )	Doping (cm <sup>-3</sup> )	Thickness ( $\mu\text{m}$ )	Doping (cm <sup>-3</sup> )	Thickness ( $\mu\text{m}$ )	Doping (cm <sup>-3</sup> )				
800	0.05	$1 \times 10^{19}$	0.06	$1 \times 10^{19}$	0.28	$2 \times 10^{17}$	8	$2.5 \times 10^{17}$	0.05	$1 \times 10^{19}$	0.03	$7 \times 10^{18}$	0.34	13.01	73.85	16.73
1000	0.02	$1 \times 10^{19}$	0.04	$6.5 \times 10^{18}$	0.15	$2 \times 10^{17}$	8	$2.5 \times 10^{17}$	0.06	$1 \times 10^{19}$	0.02	$9 \times 10^{18}$	0.40	127.25	75.03	20.07
1200	0.02	$1 \times 10^{19}$	0.03	$7.5 \times 10^{18}$	0.15	$2 \times 10^{17}$	8	$2.5 \times 10^{17}$	0.03	$1 \times 10^{19}$	0.02	$7 \times 10^{18}$	0.44	564.74	72.29	21.63
1400	0.02	$8.5 \times 10^{18}$	0.04	$3 \times 10^{17}$	0.15	$3 \times 10^{17}$	8	$2 \times 10^{17}$	0.04	$8.5 \times 10^{18}$	0.02	$9.5 \times 10^{18}$	0.46	1719.35	68.63	22.06
1600	0.02	$2 \times 10^{19}$	0.02	$5.5 \times 10^{18}$	0.11	$3 \times 10^{17}$	8	$2.5 \times 10^{17}$	0.02	$2 \times 10^{19}$	0.02	$9 \times 10^{18}$	0.49	4064.67	64.73	21.74
1800	0.03	$7 \times 10^{18}$	0.02	$9 \times 10^{18}$	0.13	$2 \times 10^{17}$	8	$2.5 \times 10^{17}$	0.03	$7 \times 10^{18}$	0.02	$9 \times 10^{18}$	0.51	8201.45	59.22	20.48
2000	0.02	$8.5 \times 10^{18}$	0.03	$1 \times 10^{19}$	0.13	$2 \times 10^{17}$	8	$4 \times 10^{17}$	0.03	$9.5 \times 10^{18}$	0.02	$8 \times 10^{18}$	0.52	14529.30	56.61	19.76

312

313 Fig. 4 illustrates the  $EQE$  of non-optimized and RCGA optimized In<sub>0.53</sub>Ga<sub>0.47</sub>As TPV cells as a  
 314 function photon  $\lambda$ . It can be seen from Fig. 4 that the  $EQE(\lambda)$  of the multi-variable optimized cell  
 315 is higher than that of the non-optimized TPV cell. This is due to the enhancement of photocurrent  
 316 generation at a wavelength higher than 0.85  $\mu\text{m}$ . A possible explanation for this is that the  
 317 optimized In<sub>0.53</sub>Ga<sub>0.47</sub>As TPV configuration tends to have higher absorption and collection of IRs  
 318 photo-generated carriers. Despite the reduction in  $V_{oc}$  by 6.52% after the optimization process,  $J_{sc}$   
 319 is significantly increased by 56.09%, resulted in the improvement in the TPV cell efficiency by  
 320 58.02%.

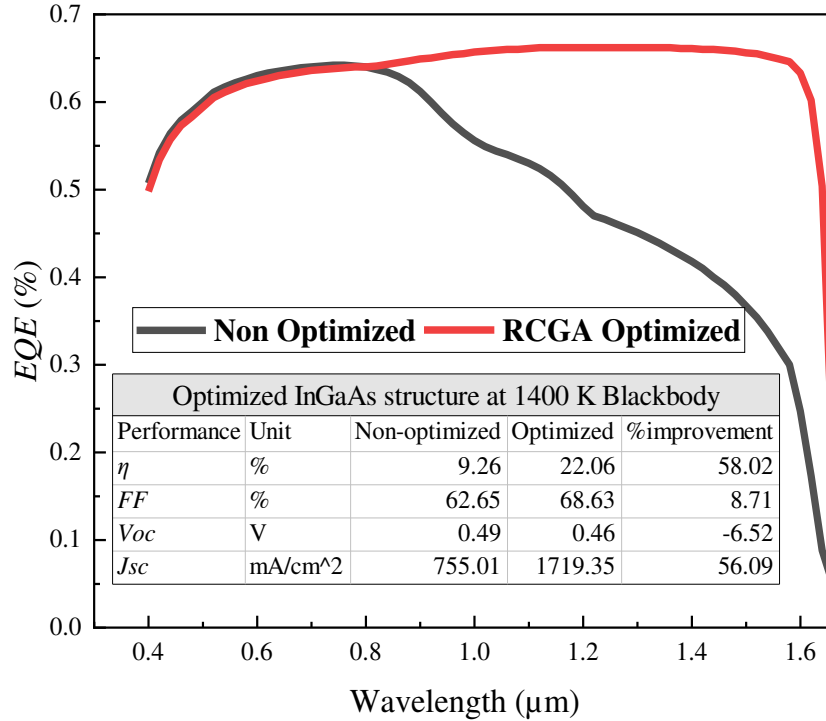


Figure 4. The external quantum efficiency vs wavelength for non-optimized and RCGA optimized In<sub>0.53</sub>Ga<sub>0.47</sub>As TPV cell under 1400 K blackbody temperature.

Based on the optimized results, a significant increase in  $\eta$  is attained when the base layer increased from 1  $\mu\text{m}$  to 8  $\mu\text{m}$ . This finding can be supported by an analysis of the absorption coefficient and the absorption length of the In<sub>0.53</sub>Ga<sub>0.47</sub>As cell. The absorption coefficient describes the light penetration in a semiconductor before being absorbed and can be obtained using Kramers-Kronig Dispersion relation as follows:

$$\alpha(\lambda) = \frac{4\pi k(\lambda)}{\lambda} (\mu\text{m}^{-1}) \quad (7)$$

where  $k(\lambda)$  is the extinction coefficient of In<sub>0.53</sub>Ga<sub>0.47</sub>As<sup>78,79</sup>. On the other hand, the absorption length ( $\alpha^{-1}$ ) is given as the inverse of the  $\alpha$  and describes the penetration length of majority photons in semiconductor before being absorbed. Due to absorption in the material, the illumination intensity weakened with increasing penetration length and can be described by means of a decaying exponential function, as shown in Equation (8)<sup>70</sup>.

337

$$\alpha_{Abs} = (1 - R).(1 - e^{-\alpha d}) \quad (8)$$

338

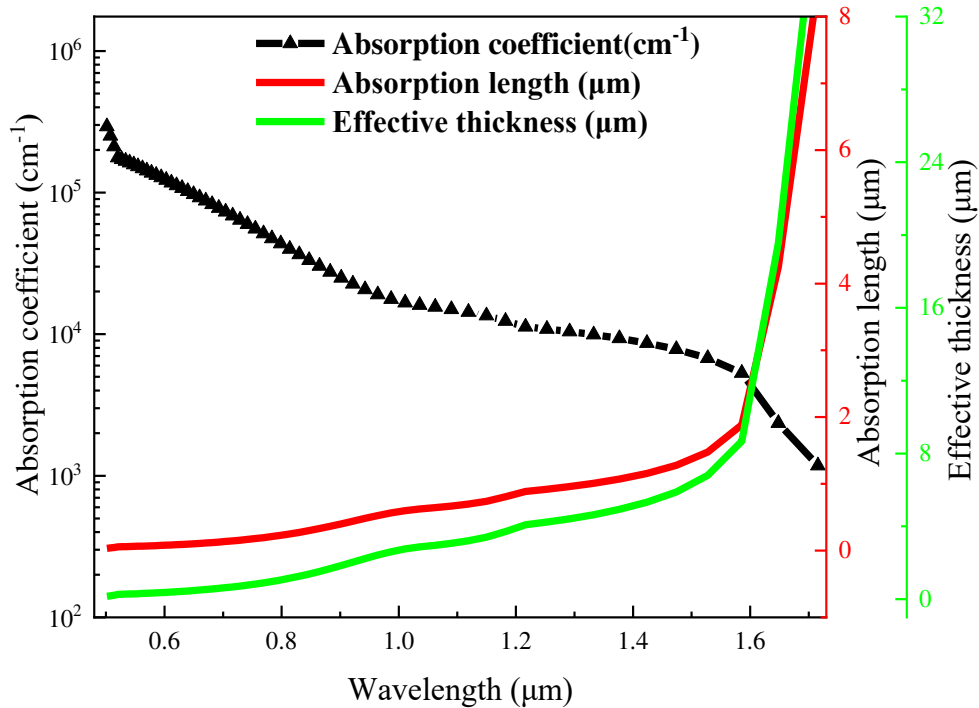
339 where  $\eta_{Abs}$  is absorption efficiency, the effective cell thickness ( $d$ ) can be determined from  
 340 Equation (9) by maximizing the absorption in the cell  $\eta_{Abs} = \sim 99\%$  and  $R = 0^{70}$ .

341

$$0.99 = (1 - e^{-\alpha d}) = 1 - 0.99 \rightarrow d = \frac{\ln(1 - 0.99)}{-\alpha} \mu\text{m} \quad (9)$$

342

343 Fig. 5 shows the result of the  $\alpha$ ,  $\alpha^{-1}$  and  $d$  of  $\text{In}_{0.53}\text{Ga}_{0.47}\text{As}$  as a function of  $\lambda$ . It can be seen that  
 344 thicker absorber layer is needed to absorb IRs. For instance, photons with  $\lambda$  of  $1.65 \mu\text{m}$  have an  
 345 absorption length of  $4.25 \mu\text{m}$ . To effectively absorb  $\sim 99\%$  of the photons, the cell thickness will  
 346 therefore be approximately  $19.59 \mu\text{m}$ .



347

348 Figure 5. The absorption coefficient, absorption length and effective thickness at different  
 349 wavelengths.

350

351 The  $\text{In}_{0.53}\text{Ga}_{0.47}\text{As}$  has a spectral response with wavelength at around  $1.75 \mu\text{m}$ . It can be seen that  
352 infrared light requires a thick absorber, so that majority of the photons are absorbed. The  
353 illumination intensity of the blackbody is mainly concentrated at  $\lambda > 1.0 \mu\text{m}$ . For instance, 1400  
354 K blackbody temperature has 69.25% of power density for wavelengths between 1 and  $1.8 \mu\text{m}$  as  
355 compared to 3.43% of power density for wavelengths between 0.2 and  $1 \mu\text{m}$ . An optical BSR is  
356 used to improve the light absorption, as the optical path distance can be doubled due to the back  
357 reflection<sup>20</sup>. Therefore, although the effective thickness to absorb photons up to  $1.75 \mu\text{m}$  is  
358 approximately  $32\text{-}36 \mu\text{m}$  (based on Fig. 5), the effective device thickness can be reduced to  
359 approximately  $16$  to  $18 \mu\text{m}$ . However, based on additional simulation work upon completing the  
360 multi-dimensional optimization, an effective thickness higher than  $8 \mu\text{m}$  (up to  $18 \mu\text{m}$ ) will only  
361 increase the efficiency by an average of about 1% for various blackbody temperatures due to the  
362 sharp decline of the absorption coefficient for  $\lambda \geq 1.63 \mu\text{m}$ . Other than that, the light trapping  
363 method such as Lambertian rear reflector and textured surface can be used to improve the light  
364 absorption in the cell<sup>70,80</sup>.

365 A further explanation for the high *EQE* is due to the effective separation and collection of  
366 generated carriers.  $\text{In}_{0.53}\text{Ga}_{0.47}\text{As}$  structure is frequently constructed with FSF and BSF layers to  
367 reduce the surface recombination and enhance the  $V_{oc}$ <sup>41,81</sup>. High to low doping concentration  
368 between the FSF or BSF and the active junction is vital to generate a SCR similar to the SCR  
369 between n-p junction. For instance, holes diffused out of this highly doped BSF layer into the  
370 lower-doped base layer, leaving site-fixed negatively charged acceptor atoms behind<sup>70</sup>. The  
371 generated electrical field that acts like an electric mirror that returns the electrons generated  
372 through absorption in the direction of the SCR<sup>70</sup>. The probability of undesired recombination at  
373 the rear of the cell is thus significantly reduced. Belghachi *et al.*<sup>82</sup> described a mathematical model  
374 on the importance of high-low junction in the front and rear sides of GaAs cell, which play a crucial  
375 role in enhancing the light-generated free carriers' collection. The thickness of FSF and BSF layers  
376 should be as thin as possible while the doping concentration should be as high as  $1 \times 10^{19} \text{cm}^{-3}$ <sup>82</sup>.  
377 The band diagram is an alternative way to view the effect of FSF and BSF layers. The band  
378 diagram of the  $\text{In}_{0.53}\text{Ga}_{0.47}\text{As}/\text{InP}$  cell was extracted from TCAD model, with the FSF and BSF  
379 layers.

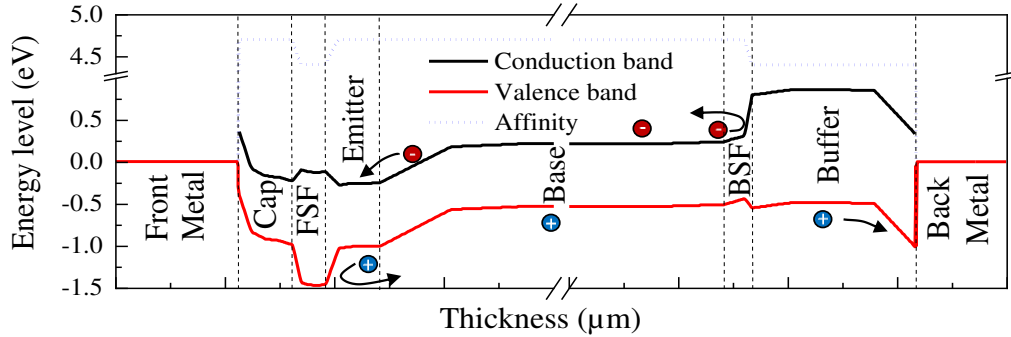


Figure 6. The band diagram of  $\text{In}_{0.53}\text{Ga}_{0.47}\text{As}$  cell heterojunction..

380  
381  
382

383 Fig. 6 presents the band diagram of  $\text{In}_{0.53}\text{Ga}_{0.47}\text{As}$  heterojunction. The band offset between  
384  $\text{In}_{0.53}\text{Ga}_{0.47}\text{As}$  and  $\text{InP}$  forms type-II band (staggered) leads to spatial separation of electrons and  
385 holes. A discontinuity in conduction for base/(BSF/buffer) interface prevents the electrons from  
386 moving further up to the back contact while allowing the flow of holes. The discontinuity in valance  
387 for the FSF/emitter interface prevents the holes from moving further up to the front contact while  
388 allowing the flow of electrons<sup>70</sup>. The band alignment of  $\text{In}_{0.53}\text{Ga}_{0.47}\text{As}$  structure was investigated in  
389 several studies<sup>83,84</sup>. The n- $\text{InP}$  will form a barrier to holes, but a sink for electrons at the FSF and visa  
390 verse at the BSF/buffer. Besides that, cell total voltage is now divided into the potential level at n-p  
391 junction and additional level at  $n^+n$  and  $pp^+$  interfaces<sup>70</sup>. Hence, FSF layer improves the *EQE* of  
392 shorter wavelengths photo-generated carriers, and the BSF/buffer layer increases the *EQE* of longer  
393 wavelengths photo-generated carriers<sup>82</sup>. It should be stressed that BSF/buffer layer is very significant  
394 to enhance the  $J_{sc}$  and  $V_{oc}$  of the TPV cell since the long-wavelength photons tend to absorb at the  
395 deeper region of the structure. The combination of both thicker absorber layer and BSF/buffer  
396 significantly improves the collection of photocurrent collection of  $\lambda$  near to the band-edge of  
397  $\text{In}_{0.53}\text{Ga}_{0.47}\text{As}$  TPV cell.

### 398 **Conclusion.**

399 In summary, the simulation model is validated with reported experimental data, generating a low  $\eta$   
400 percentage error of 0.61% between experimental and simulation. Research gap was identified based  
401 on comprehensive comparison of previous structure designs and performance of  $\text{In}_{0.53}\text{Ga}_{0.47}\text{As}$  cell.  
402 Single variable and multi-dimensional optimization (RCGA) of heterojunction  $\text{In}_{0.53}\text{Ga}_{0.47}\text{As}$  cell are  
403 developed and applied under 800 to 2000 K TPV radiation temperatures. The single variable

404 optimization is used to investigate the effect of thickness and doping concentration of layers, which  
405 demonstrated the significant impact of the base layer to achieve high performance  $\text{In}_{0.53}\text{Ga}_{0.47}\text{As}$   
406 TPV cell. Meanwhile, under radiation temperatures ranging from 800 K to 2000 K, optimized  
407  $\text{In}_{0.53}\text{Ga}_{0.47}\text{As}$  heterojunction TPV cell using RCGA increases the  $\eta$  by an average of 11.86% as  
408 compared to the reference structure. It was found that the incorporation of a thicker absorber with  
409 effective barrier layer BSF/Buffer layer improves the absorption and collection of photo-generated  
410 carriers near the band-edge, which produced higher output performance. The increment of the  
411  $\text{In}_{0.53}\text{Ga}_{0.47}\text{As}$  cell efficiency leads to a significant increase in the generated output power,  
412 demonstrating great potential of TPV for industrial waste heat harvesting. Finally, the method of  
413 hybridizing the Silvaco TCAD software with RCGA for multi-dimensional optimization can be  
414 readily adopted in optimization work for semiconductor devices, such as solar cell, TPV cell and  
415 photodetectors.

## References

1. Wang, X., Liang, R., Fisher, P., Chan, W. & Xu, J. Radioisotope Thermophotovoltaic Generator Design Methods and Performance Estimates for Space Missions. *J. Propuls. Power* **36**, 593–603 (2020).
2. Fraas, L. M. *Thermophotovoltaics Using Infrared Sensitive Cells in Low-Cost Solar Electric Power*. Springer, Cham (Springer International Publishing, 2014). doi:10.1007/978-3-319-07530-3.
3. Fraas L, M Avery J, E Huang H, X Martinelli R, U. Thermophotovoltaic system configurations and spectral control. *Semicond. Sci. Technol.* **18**, S165–S173 (2003).
4. Schock, A., Or, C. & Kumar, V. Design and integration of small RTPV generators with new millennium spacecraft for outer solar system. *Acta Astronaut.* **41**, 801–816 (1997).
5. Krier, A., Yin, M., Marshall, A. R. J. & Krier, S. E. Low Bandgap InAs-Based Thermophotovoltaic Cells for Heat-Electricity Conversion. *J. Electron. Mater.* **45**, 2826–2830 (2016).
6. Lenert, A. *et al.* A nanophotonic solar thermophotovoltaic device. *Nat. Nanotechnol.* **9**, 126–130 (2014).
7. Elzouka, M. & Ndao, S. Towards a near-field concentrated solar thermophotovoltaic microsystem: Part I – Modeling. *Sol. Energy* **141**, 323–333 (2017).
8. A. Datas, C. A. Development and experimental evaluation of a complete solar thermophotovoltaic system. *Prog. PHOTOVOLTAICS Res. Appl.* **15**, 326–334 (2012).
9. Amy, C., Seyf, H. R., Steiner, M. A., Friedman, D. J. & Henry, A. Thermal energy grid storage using multi-junction photovoltaics. *Energy Environ. Sci.* **12**, 334–343 (2019).
10. Seyf, H. R. & Henry, A. Thermophotovoltaics: a potential pathway to high efficiency concentrated solar power. *Energy Environ. Sci.* **9**, 2654–2665 (2016).
11. Seal, M., Christ, S., Campbell, G., West, E. & Fraas, L. Thermophotovoltaic Generation of Power for Use in a Series Hybrid Vehicle. in *SAE Technical Papers* vol. 56 55–8 (1997).

12. Utlu, Z. & Önal, B. S. Thermodynamic analysis of thermophotovoltaic systems used in waste heat recovery systems: An application. *Int. J. Low-Carbon Technol.* **13**, 52–60 (2018).
13. Fraas, L. M. Economic potential for thermophotovoltaic electric power generation in the steel industry. in *2014 IEEE 40th Photovoltaic Specialist Conference, PVSC 2014* 766–770 (2014). doi:10.1109/PVSC.2014.6925031.
14. Shan, S., Zhou, Z. & Cen, K. An innovative integrated system concept between oxy-fuel thermo-photovoltaic device and a Brayton-Rankine combined cycle and its preliminary thermodynamic analysis. *Energy Convers. Manag.* **180**, 1139–1152 (2019).
15. Rashid, W. E. S. W. A. *et al.* Recent Development of Thermophotovoltaic System for Waste Heat Harvesting Application and Potential Implementation in Thermal Power Plant. *IEEE Access* **8**, 105156–105168 (2020).
16. Yang, Z. *et al.* An efficient method exploiting the waste heat from a direct carbon fuel cell by means of a thermophotovoltaic cell. *Energy Convers. Manag.* **149**, 424–431 (2017).
17. Van der Heide, J., Posthuma, N. E., Flamand, G., Geens, W. & Poortmans, J. Cost-efficient thermophotovoltaic cells based on germanium substrates. *Sol. Energy Mater. Sol. Cells* **93**, 1810–1816 (2009).
18. Lotfi, H. *et al.* Narrow-Bandgap Interband Cascade Thermophotovoltaic Cells. *IEEE J. Photovoltaics* **7**, 1462–1468 (2017).
19. Bett, A. W. & Sulima, O. V. GaSb photovoltaic cells for applications in TPV generators. *Semicond. Sci. Technol.* **18**, S184–S190 (2003).
20. Burger, T., Fan, D., Lee, K., Forrest, S. R. & Lenert, A. Thin-Film Architectures with High Spectral Selectivity for Thermophotovoltaic Cells. *ACS Photonics* **5**, 2748–2754 (2018).
21. Hitchcock, C. W., Gutmann, R. J. & Borrego, J. M. Antimonide-based devices for thermophotovoltaic applications. *IEEE Trans. Electron Devices* **46**, 2154–2161 (1999).
22. Choi, H. K. *et al.* High-performance GaInAsSb thermophotovoltaic devices with an AlGaAsSb window. *Appl. Phys. Lett.* **71**, 3758–3760 (1997).

23. Mauk, M. G., Tata, A. N. & Cox, J. A. Solution growth of thick III-V antimonide alloy epilayers (InAsSb, InGaSb, InGaAsSb, AlGaAsSb, and InAsSbP) for ‘virtual substrates’. *J. Cryst. Growth* **225**, 236–243 (2001).
24. Bitnar, B., Durisch, W. & Holzner, R. Thermophotovoltaics on the move to applications. *Appl. Energy* **105**, 430–438 (2013).
25. Bauer, T. *Thermophotovoltaics. Green Energy and Technology* vol. 7 (Springer Berlin Heidelberg, 2011).
26. Kao, Y.-C. *et al.* Performance comparison of III–V//Si and III–V//InGaAs multi-junction solar cells fabricated by the combination of mechanical stacking and wire bonding. *Sci. Rep.* **9**, 4308 (2019).
27. Sodabanlu, H., Watanabe, K., Sugiyama, M. & Nakano, Y. Growth of InGaAs(P) in planetary metalorganic vapor phase epitaxy reactor using tertiarybutylarsine and tertiarybutylphosphine for photovoltaic applications. *Jpn. J. Appl. Phys.* **57**, 08RD09 (2018).
28. Yamada, T. *et al.* 5 × 5 cm<sup>2</sup> GaAs and GaInAs solar cells with high conversion efficiency. *Japanese J. Appl. Physics, Part 2 Lett.* **44**, 7–10 (2005).
29. Wilt, D. M. *et al.* High efficiency indium gallium arsenide photovoltaic devices for thermophotovoltaic power systems. *Appl. Phys. Lett.* **64**, 2415–2417 (1994).
30. Zahler, J. M. *et al.* High efficiency InGaAs solar cells on Si by InP layer transfer. *Appl. Phys. Lett.* **91**, 012108 (2007).
31. Dharmarasu, N. *et al.* High-radiation-resistant InGaP, InGaAsP, and InGaAs solar cells for multijunction solar cells. *Appl. Phys. Lett.* **79**, 2399–2401 (2001).
32. Omair, Z. *et al.* Ultraefficient thermophotovoltaic power conversion by band-edge spectral filtering. *Proc. Natl. Acad. Sci.* **116**, 15356–15361 (2019).
33. Crystals, J. <http://jxcrystals.com/GaSb/4sale5.pdf>. 1–2.
34. Bauhuis, G. J., Mulder, P., Haverkamp, E. J., Huijben, J. C. C. M. & Schermer, J. J. 26.1% thin-film GaAs solar cell using epitaxial lift-off. *Sol. Energy Mater. Sol. Cells* **93**, 1488–

- 1491 (2009).
35. Emziane, M. & Nicholas, R. J. Optimization of InGaAs(P) photovoltaic cells lattice matched to InP. *J. Appl. Phys.* **101**, 054503 (2007).
  36. Tuley, R. S. & Nicholas, R. J. Band gap dependent thermophotovoltaic device performance using the InGaAs and InGaAsP material system. *J. Appl. Phys.* (2010) doi:10.1063/1.3488903.
  37. Tan, M. *et al.* Investigation of InGaAs thermophotovoltaic cells under blackbody radiation. *Appl. Phys. Express* **7**, 096601 (2014).
  38. Tuley, R. S. *et al.* Lattice-matched InGaAs on InP thermophotovoltaic cells. *Semicond. Sci. Technol.* **28**, 015013 (2013).
  39. Emziane, M. & Nicholas, R. J. Optimization of InGaAs(P) photovoltaic cells lattice matched to InP. *J. Appl. Phys.* **101**, 054503 (2007).
  40. Karlina, L. B., Vlasov, A. S., Kulagina, M. M. & Timoshina, N. K. Thermophotovoltaic cells based on In<sub>0.53</sub>Ga<sub>0.47</sub>As/InP heterostructures. *Semiconductors* **40**, 346–350 (2006).
  41. Kim, C.-Y., Cha, J.-H., Kim, J. & Kwon, Y.-S. Open-Circuit Voltage Improvement in InGaAs/InP Heterojunction Solar Cells. *Jpn. J. Appl. Phys.* **44**, 2523–2524 (2005).
  42. Matsubara, H., Tanabe, T., Moto, A., Mine, Y. & Takagishi, S. Over 27% efficiency GaAs/InGaAs mechanically stacked solar cell. *Sol. Energy Mater. Sol. Cells* **50**, 177–184 (1998).
  43. Wilt, D. M. *et al.* Electrical and optical performance characteristics of p/n InGaAs monolithic interconnected modules. *NASA Lewis Res. Cent.* 1119–1124 (1997).
  44. Wojtczuk, S., Gagnon, E., Geoffroy, L. & Parodos, T. In<sub>x</sub>Ga<sub>1-x</sub>As thermophotovoltaic cell performance vs bandgap. *AIP Conf. Proc.* **321**, 177–187 (1995).
  45. Baloch, A. A. B. *et al.* Full space device optimization for solar cells. *Sci. Rep.* **7**, 11984 (2017).
  46. Baudrit, M. & Algora, C. Theoretical optimization of GaInP/GaAs dual-junction solar cell: Toward a 36% efficiency at 1000 suns. *Phys. Status Solidi Appl. Mater. Sci.* **207**, 474–478

- (2010).
47. Levinshtein, M., Rumyantsev, S. & Shur, M. *Handbook Series on Semiconductor Parameters: Ternary And Quaternary III-V Compounds*. vol. 2 (World Scientific Publishing Co. Pte. Ltd., 1996).
  48. Jurczak, P., Onno, A., Sablon, K. & Liu, H. Efficiency of GaInAs thermophotovoltaic cells: the effects of incident radiation, light trapping and recombinations. *Opt. Express* **23**, A1208 (2015).
  49. Salem, A. F. & Brennan, K. F. Theoretical study of the response of InGaAs metal-semiconductor-metal photodetectors. *IEEE J. Quantum Electron.* **31**, 944–953 (1995).
  50. Datta, S., Roenker, K. P., Cahay, M. M. & Stanchina, W. E. Implications of hole vs electron transport properties for high speed Pnp heterojunction bipolar transistors. *Solid. State. Electron.* **43**, 73–79 (1999).
  51. Sotoodeh, M., Khalid, A. H. & Rezazadeh, A. A. Empirical low-field mobility model for III-V compounds applicable in device simulation codes. *J. Appl. Phys.* **87**, 2890–2900 (2000).
  52. Menon, P. S., Kandiah, K. & Shaari, S. Concentration and temperature-dependent low-field mobility model for  $\text{In}_{0.53}\text{Ga}_{0.47}\text{As}$  interdigitated lateral pin PD. *IEICE Electron. Express* **5**, 303–309 (2008).
  53. Ahrenkiel, R. K., Ellingson, R., Johnston, S. & Wanlass, M. Recombination lifetime of  $\text{In}_{0.53}\text{Ga}_{0.47}\text{As}$  as a function of doping density. *Appl. Phys. Lett.* **72**, 3470–3472 (1998).
  54. Zemel, A. & Gallant, M. Carrier lifetime in  $\text{InP}/\text{InGaAs}/\text{InP}$  by open-circuit voltage and photoluminescence decay. *J. Appl. Phys.* **78**, 1094–1100 (1995).
  55. Chiang, H., Rode, J. C., Choudhary, P. & Rodwell, M. J. W. Lateral carrier diffusion and current gain in terahertz  $\text{InGaAs}/\text{InP}$  double-heterojunction bipolar transistors. *J. Appl. Phys.* **115**, 034513 (2014).
  56. Cui, D., Hubbard, S. M., Pavlidis, D., Eisenbach, A. & Chelli, C. Impact of doping and MOCVD conditions on minority carrier lifetime of zinc- and carbon-doped  $\text{InGaAs}$  and its

- applications to zinc- and carbon-doped InP/InGaAs heterostructure bipolar transistors. *Semicond. Sci. Technol.* **17**, 503–509 (2002).
57. Zeng, Q. Y. *et al.* Dependence of dark current on carrier lifetime for InGaAs/InP avalanche photodiodes. *Opt. Quantum Electron.* **47**, 1671–1677 (2015).
  58. Woolf, D. N. *et al.* High-efficiency thermophotovoltaic energy conversion enabled by a metamaterial selective emitter. *Optica* **5**, 213–218 (2018).
  59. Liu, X. *et al.* Taming the Blackbody with Infrared Metamaterials as Selective Thermal Emitters. *Phys. Rev. Lett.* **107**, 045901 (2011).
  60. Tong, J. K., Hsu, W. C., Huang, Y., Boriskina, S. V. & Chen, G. Thin-film ‘thermal well’ emitters and absorbers for high-efficiency thermophotovoltaics. *Sci. Rep.* **5**, 1–12 (2015).
  61. Dawoud, B., Amer, E. & Gross, D. Experimental investigation of an adsorptive thermal energy storage. *Int. J. energy Res.* **31**, 135–147 (2007).
  62. Fourspring, P. M., DePoy, D. M., Rahmlow, T. D., Lazo-Wasem, J. E. & Gratrix, E. J. Optical coatings for thermophotovoltaic spectral control. *Appl. Opt.* **45**, 1356–1358 (2006).
  63. Chuang, Y.-C., Chen, C.-T. & Hwang, C. A simple and efficient real-coded genetic algorithm for constrained optimization. *Appl. Soft Comput.* **38**, 87–105 (2016).
  64. Hassanat, A. *et al.* Choosing Mutation and Crossover Ratios for Genetic Algorithms—A Review with a New Dynamic Approach. *Information* **10**, 390 (2019).
  65. Kayes, B. M. *et al.* 27.6% Conversion efficiency, a new record for single-junction solar cells under 1 sun illumination. in *2011 37th IEEE Photovoltaic Specialists Conference* vol. 28 000004–000008 (IEEE, 2011).
  66. Zhou, H., Qu, Y., Zeid, T. & Duan, X. Towards highly efficient photocatalysts using semiconductor nanoarchitectures. *Energy Environ. Sci.* **5**, 6732–6743 (2012).
  67. Olmsted, N. & Record, C. InP Solar Cell With Window Layer. *United States Patent 19* (1994).
  68. Green, M. A. *Solar Cells: Operating Principles, Technology and System Applications.* (University of New South Wales, 1986).

69. Wu, F. L., Ou, S. L., Horng, R. H. & Kao, Y. C. Improvement in separation rate of epitaxial lift-off by hydrophilic solvent for GaAs solar cell applications. *Sol. Energy Mater. Sol. Cells* **122**, 233–240 (2014).
70. Konrad Mertens. Structure and Method of Operation of Solar Cells. in *Photovoltaics : Fundamentals, Technology and Practice* (2014). doi:10.1007/978-3-319-29650-0\_7.
71. Yubo Sun *et al.* Modeling wide bandgap GaInP photovoltaic cells for conversion efficiencies up to 16.5%. in *2015 IEEE 42nd Photovoltaic Specialist Conference (PVSC)* 1–6 (IEEE, 2015). doi:10.1109/PVSC.2015.7356074.
72. Andreani, L. C., Bozzola, A., Kowalczewski, P., Liscidini, M. & Redorici, L. Silicon solar cells: Toward the efficiency limits. *Adv. Phys. X* **4**, (2019).
73. Wilt, D., Wehrer, R., Palmisiano, M., Wanlass, M. & Murray, C. Monolithic interconnected modules (MIMs) for thermophotovoltaic energy conversion. *Semicond. Sci. Technol.* **18**, S209–S215 (2003).
74. Karalis, A. & Joannopoulos, J. D. Squeezing' near-field thermal emission for ultra-efficient high-power thermophotovoltaic conversion. *Sci. Rep.* **6**, 1–12 (2016).
75. Fan, D. *et al.* Near-perfect photon utilization in an air-bridge thermophotovoltaic cell. *Nature* **586**, 237–241 (2020).
76. Mathews, I. *et al.* InAlAs and InGaAs solar cell development for use in monolithic triple-junction solar cells with improved spectrum splitting. in *28th European Photovoltaic Solar Energy Conference and Exhibition* (2013). doi:110.4229/28thEUPVSEC2013-1AV.2.40.
77. Alharbi, F. H. *et al.* An efficient descriptor model for designing materials for solar cells. *npj Comput. Mater.* **1**, 15003 (2015).
78. Adachi, S. Optical dispersion relations for GaP, GaAs, GaSb, InP, InAs, InSb, Al<sub>x</sub>Ga<sub>1-x</sub>As, and In<sub>1-x</sub>Ga<sub>x</sub>As<sub>y</sub>P<sub>1-y</sub>. *J. Appl. Phys.* **66**, 6030–6040 (1989).
79. Nee, T. W. & Green, A. K. Optical properties of InGaAs lattice-matched to InP. *J. Appl. Phys.* **68**, 5314–5317 (1990).
80. Kim, Y., Lam, N. D., Kim, K., Park, W.-K. & Lee, J. Ge nanopillar solar cells epitaxially

grown by metalorganic chemical vapor deposition. *Sci. Rep.* **7**, 42693 (2017).

81. Gamel, M. *et al.* Effect of Front-Surface-Field and Back-Surface-Field on the Performance of GaAs Based-Photovoltaic Cell. in *2019 IEEE International Conference on Sensors and Nanotechnology* 1–4 (IEEE, 2019). doi:10.1109/SENSORSNANO44414.2019.8940098.
82. Belghachi, A. & Helmaoui, A. Effect of the front surface field on GaAs solar cell photocurrent. *Sol. Energy Mater. Sol. Cells* **92**, 667–672 (2008).
83. Loga, R., Loga, R. & Vilches, A. Fabrication and characterization of circular geometry InP/InGaAs double heterojunction bipolar transistors. *Semicond. Sci. Technol.* **19**, 855–858 (2004).
84. Ginige, R., Cherkaoui, K., Wong Kwan, V., Kelleher, C. & Corbett, B. High injection and carrier pile-up in lattice matched InGaAs/InP PN diodes for thermophotovoltaic applications. *J. Appl. Phys.* **95**, 2809–2815 (2004).

### **Acknowledgements**

The authors gratefully acknowledge the Tenaga Nasional Berhad (TNB) seeding fund (Project code: U-TG-RD-18-04).

### **Author contributions**

M. M. A. G., P. J. K and H. J. L. designed the research; M. M. A. G., P. J. K., H. J. L. and W. E. S. W. A. R. performed the optimization, analyzed the data and wrote the manuscript and M. A. H., J. P. R. D. and M. Z. J. provided study oversight and edited the manuscript. All authors discussed the results and commented on the manuscript.

### **Competing interests**

The authors declare no competing interests.

# Figures

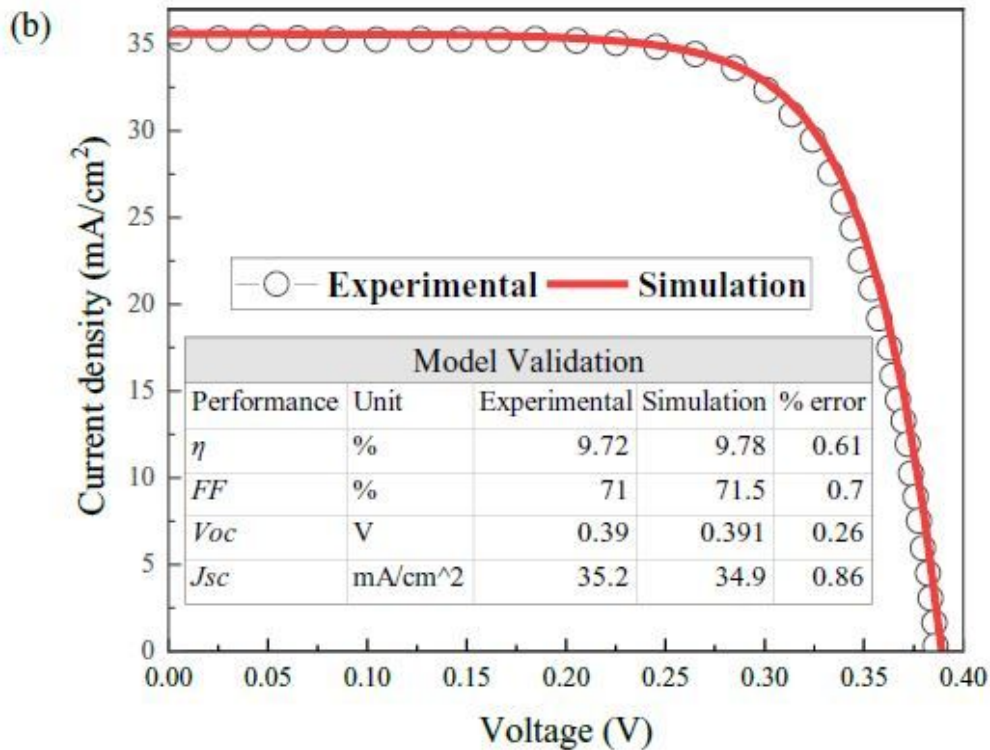
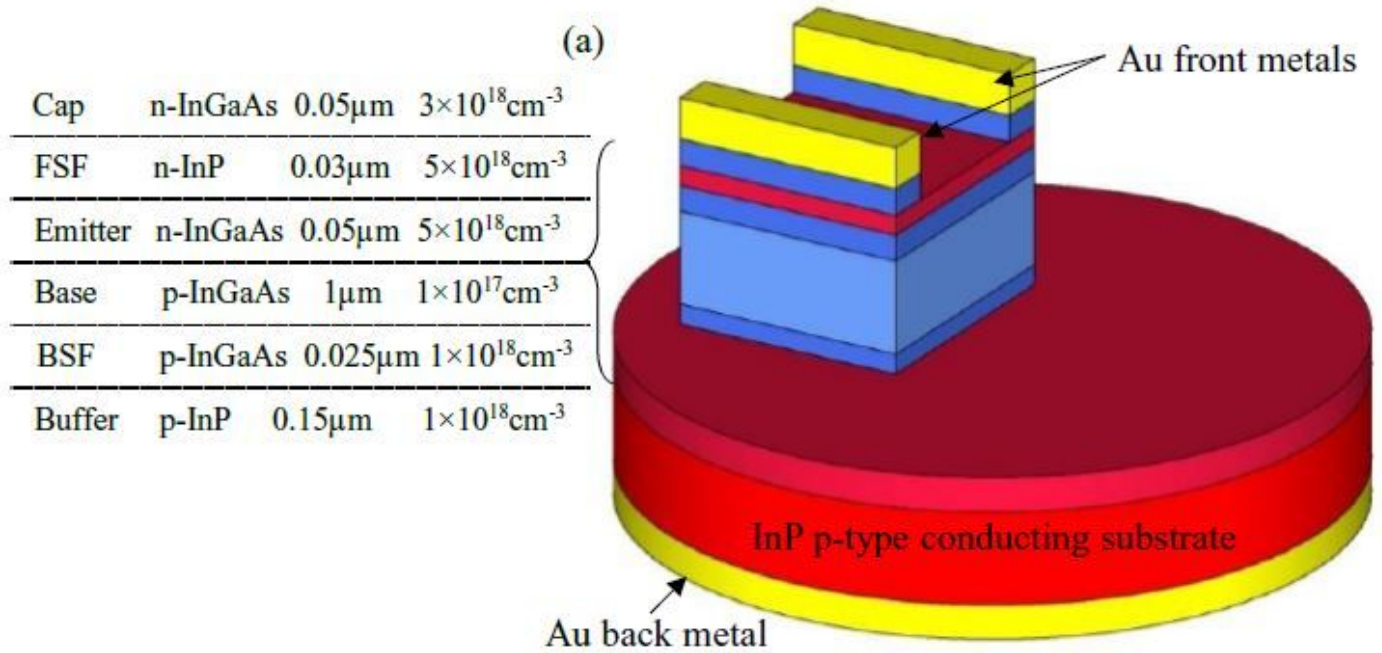
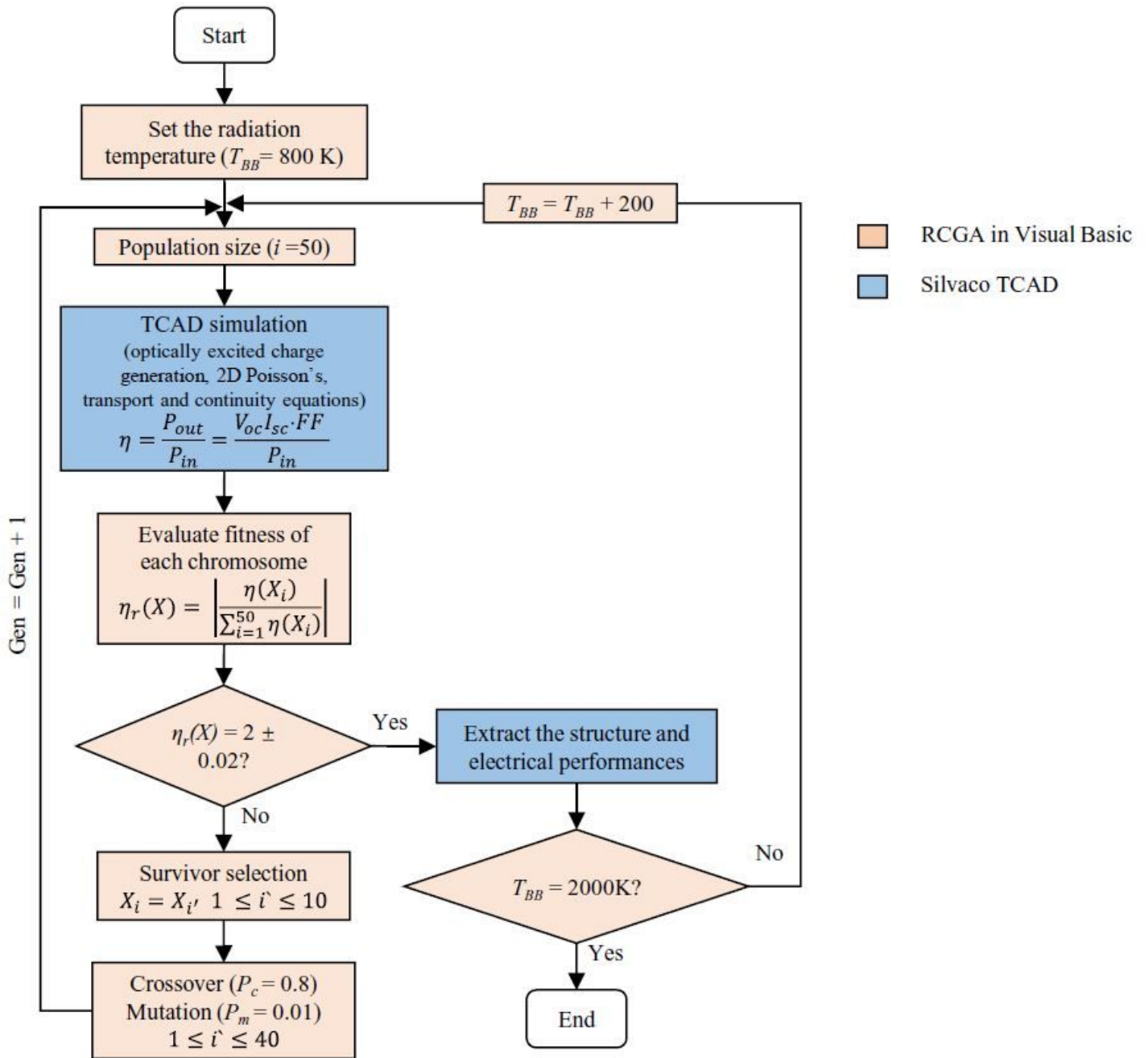


Figure 1

Simulation to reported experimental of In<sub>0.53</sub>Ga<sub>0.47</sub>As (a) Baseline n-p structure27 (b) JV curve and performance parameters.



**Figure 2**

The flowchart that illustrates the hybridization of Silvaco TCAD with Real coded genetic algorithm.

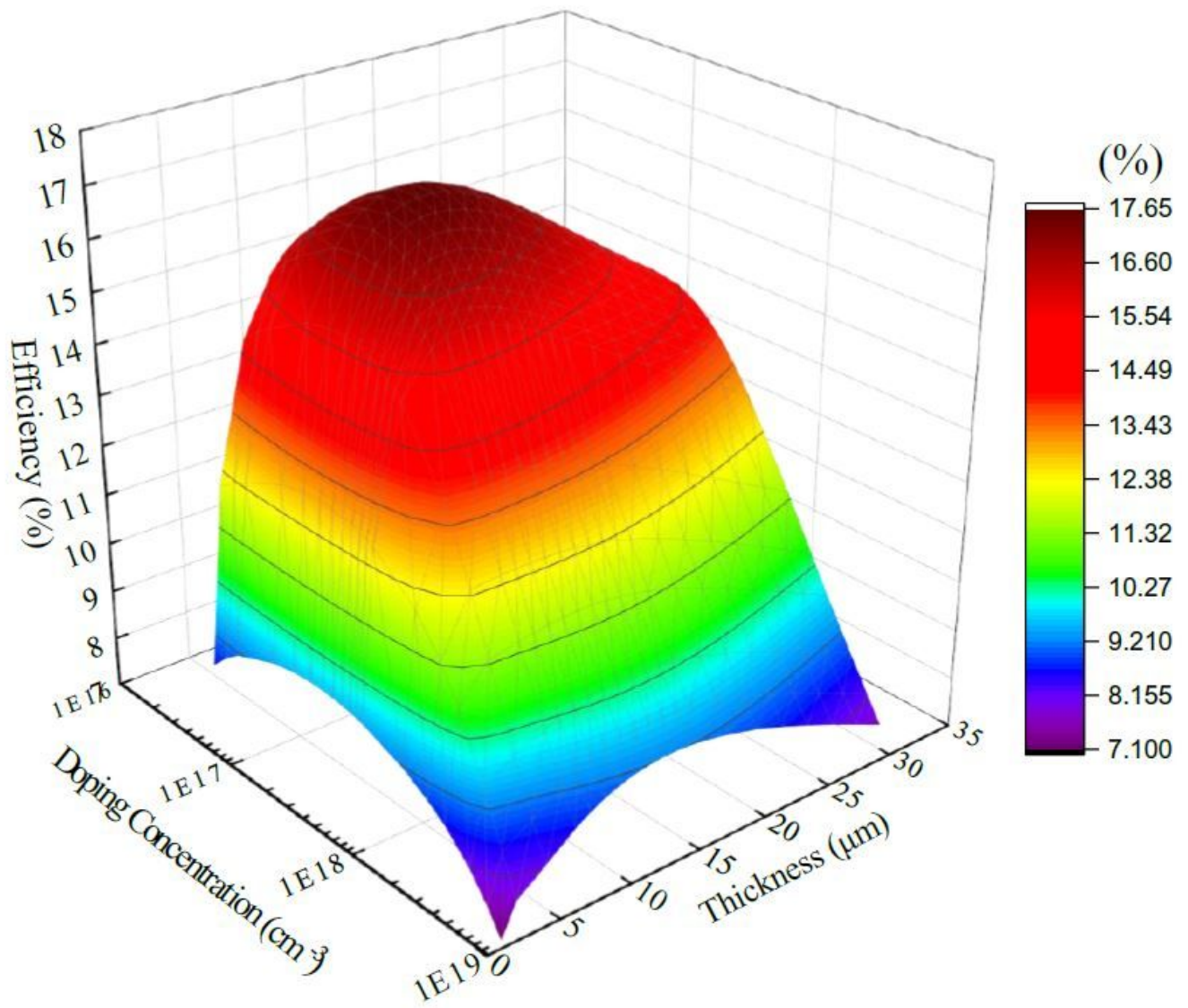


**Figure 3**

The efficiency of In<sub>0.53</sub>Ga<sub>0.47</sub>As TPV cell vs thickness and doping concentration of the base layer under 1400 K blackbody temperature.

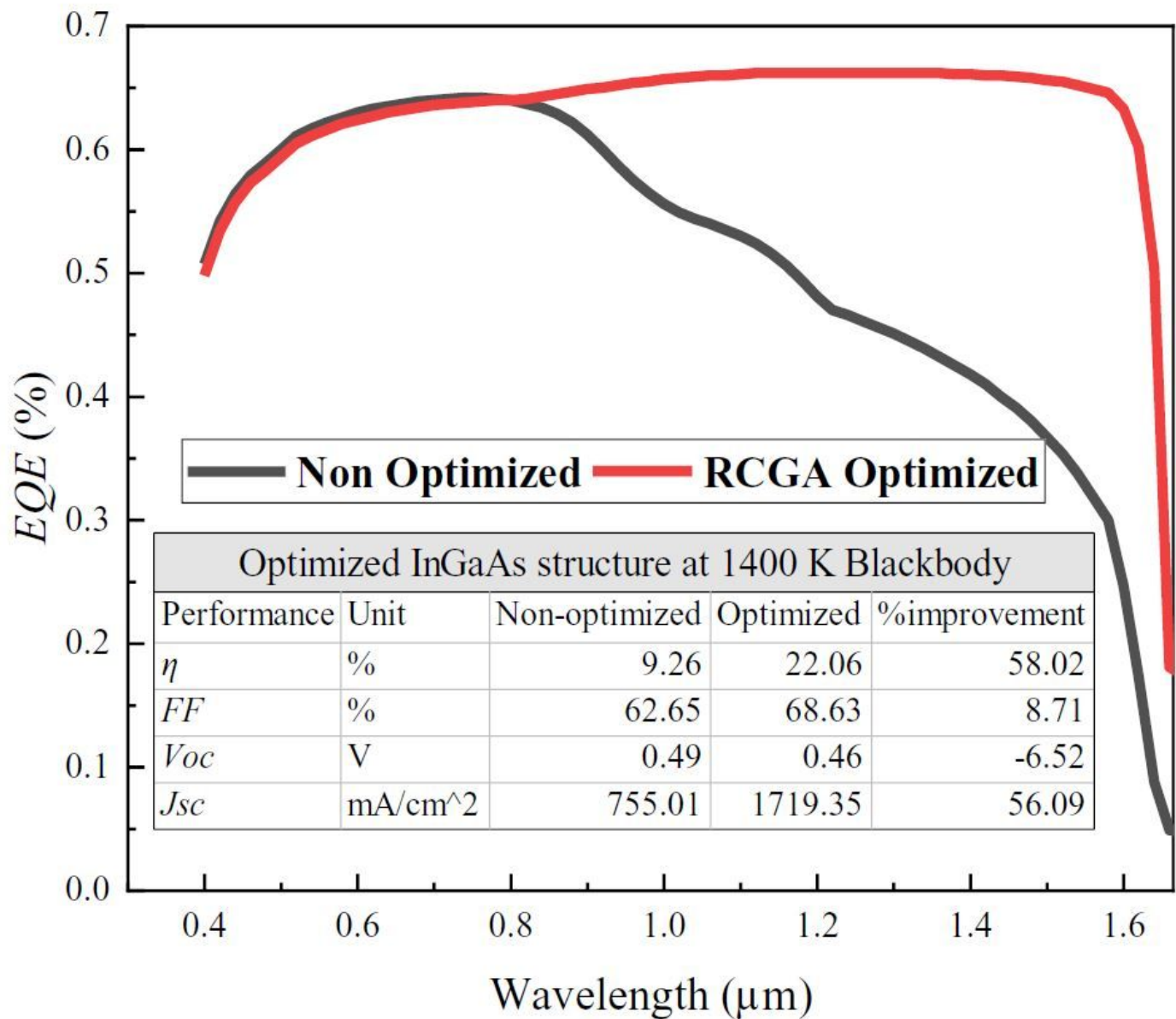


**Figure 4**

The external quantum efficiency vs wavelength for non-optimized and RCGA optimized In<sub>0.53</sub>Ga<sub>0.47</sub>As TPV cell under 1400 K blackbody temperature.

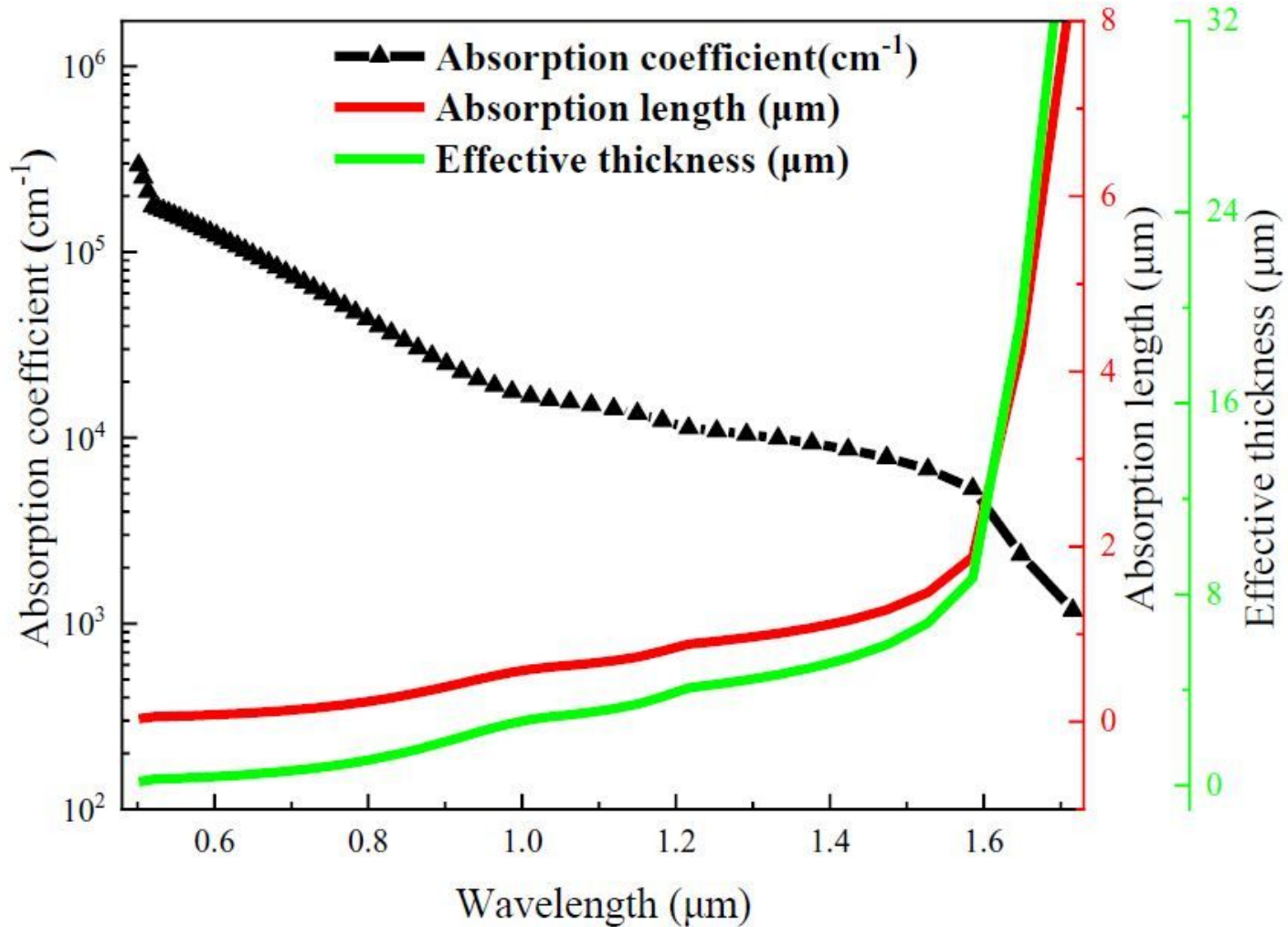


Figure 5

The absorption coefficient, absorption length and effective thickness at different wavelengths.

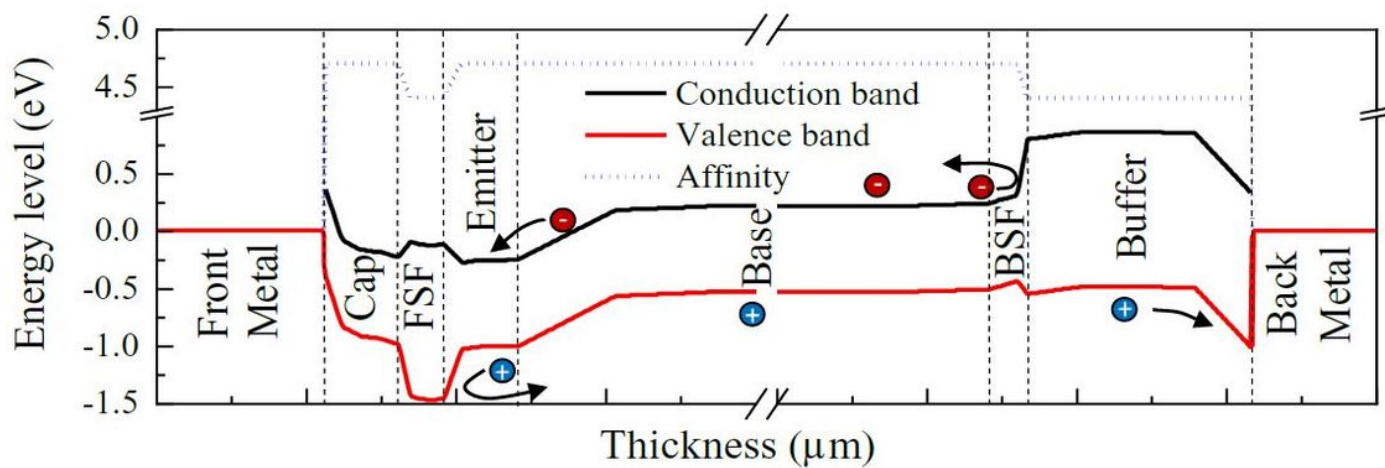


Figure 6

The band diagram of  $\text{In}_{0.53}\text{Ga}_{0.47}\text{As}$  cell heterojunction..